Monthly Notices of the ROYAL ASTRONOMICAL SOCIETY

MNRAS **468,** 4642–4662 (2017) doi:10.1093/mnras/stx834
Advance Access publication 2017 April 4

Complexity in the light curves and spectra of slow-evolving superluminous supernovae

C. Inserra,[1,2⋆] M. Nicholl,[3] T.-W. Chen,[4] A. Jerkstrand,[5] S. J. Smartt,[1] T. Krühler,[4] J. P. Anderson,[6] C. Baltay,[7] M. Della Valle,[8] M. Fraser,[9] A. Gal-Yam,[10] L. Galbany,[11] E. Kankare,[1] K. Maguire,[1] D. Rabinowitz,[7] K. Smith,[1] S. Valenti[12] and D. R. Young[1]

[1]*Astrophysics Research Centre, School of Mathematics and Physics, Queen's University Belfast, Belfast BT7 1NN, UK*
[2]*Department of Physics & Astronomy, University of Southampton, Southampton, Hampshire, SO17 1BJ, UK*
[3]*Harvard-Smithsonian Center for Astrophysics, 60 Garden Street, Cambridge, MA 02138, USA*
[4]*Max-Planck-Institut für Extraterrestrische Physik, Giessenbachstraße 1, D-85748 Garching, Germany*
[5]*Max Planck Institute for Astrophysics, Garching, Karl-Schwarzschild-Str. 1, Postfach 1317, D-85741 Garching, Germany*
[6]*European Southern Observatory, Alonso de Córdova 3107, Vitacura, Casilla 190001, Santiago, Chile*
[7]*Physics Department, Yale university, New Haven, CT 06511, USA*
[8]*Capodimonte Observatory, Salita Moiariello 16, I-80131 Napoli, Italy*
[9]*School of Physics, O'Brien Centre for Science North, University College Dublin, Belfield, Dublin 4, Ireland*
[10]*Benoziyo Center for Astrophysics, Weizmann Institute of Science, 76100 Rehovot, Israel*
[11]*Physics and Astronomy Department, University of Pittsburgh, Pittsburgh, PA 15260, USA*
[12]*Department of Physics, University of California Davis, 1 Shields Ave, Davis, CA 95616, USA*

Accepted 2017 March 31. Received 2017 February 25; in original form 2016 December 19

ABSTRACT

A small group of the newly discovered superluminous supernovae show broad and slow-evolving light curves. Here we present extensive observational data for the slow-evolving superluminous supernova LSQ14an, which brings this group of transients to four in total in the low-redshift Universe ($z < 0.2$; SN 2007bi, PTF12dam, SN 2015bn). We particularly focus on the optical and near-infrared evolution during the period from 50 d up to 400 d from peak, showing that they are all fairly similar in their light curve and spectral evolution. LSQ14an shows broad, blueshifted [O III] λλ4959, 5007 lines, as well as a blueshifted [O II] λλ7320, 7330 and [Ca II] λλ7291, 7323. Furthermore, the sample of these four objects shows common features. Semi-forbidden and forbidden emission lines appear surprisingly early at 50–70 d and remain visible with almost no variation up to 400 d. The spectra remain blue out to 400 d. There are small, but discernible light-curve fluctuations in all of them. The light curve of each shows a faster decline than ^{56}Co after 150 d and it further steepens after 300 d. We also expand our analysis presenting X-ray limits for LSQ14an and SN 2015bn and discuss their diagnostic power. These features are quite distinct from the faster evolving superluminous supernovae and are not easily explained in terms of only a variation in ejecta mass. While a central engine is still the most likely luminosity source, it appears that the ejecta structure is complex, with multiple emitting zones and *at least* some interaction between the expanding ejecta and surrounding material.

Key words: stars: mass-loss – supernovae: individual: LSQ14an – supernovae: individual: SN2015bn – supernovae: individual: PTF12dam – supernovae: individual: SN2007bi – X-rays: general.

1 INTRODUCTION

A new class of intrinsically bright supernovae (SNe), labelled superluminous supernovae (SLSNe; Quimby et al. 2011; Gal-Yam 2012), was unveiled during last decade. They were originally identified as those SNe showing $M \sim -21$ mag (e.g. Smith et al. 2007; Pastorello et al. 2010; Chomiuk et al. 2011; Quimby et al. 2011; Gal-Yam 2012; Howell et al. 2013; Inserra et al. 2013) and divided into three different types (see the early review of Gal-Yam 2012). They now tend to be separated and classified based on their spectrophotometric behaviour rather than a simple magnitude threshold (e.g.

⋆ E-mail: C.Inserra@soton.ac.uk

Papadopoulos et al. 2015; Inserra et al. 2016b; Lunnan et al. 2016; Prajs et al. 2017). Those exhibiting hydrogen-free ejecta are grouped together as SLSNe I, while those showing hydrogen as SLSNe II.

SLSNe I, although intrinsically rare (Quimby et al. 2013; McCrum et al. 2015; Prajs et al. 2017), are the most commonly studied and usually found in dwarf, metal-poor galaxies (e.g. Lunnan et al. 2014; Leloudas et al. 2015a; Angus et al. 2016; Chen et al. 2016; Perley et al. 2016). At about 30 d after peak, these SNe tend to show strong resemblances to normal or broad-lined Type Ic SNe at peak luminosity (e.g. Pastorello et al. 2010; Liu & Modjaz 2016) and thus are also usually referred to as SLSNe Ic (e.g. Inserra et al. 2013; Nicholl et al. 2013). Their light curves show significant differences in width and temporal evolution with the rise times being correlated with the decline rates (Nicholl et al. 2015b). Whether or not there are two distinct groups, and two different physical mechanisms for the fast-evolving (e.g. SN 2010gx) and slow-evolving (e.g. SN 2007bi) explosions remains to be seen.

In addition, thanks to modern imaging surveys, we have been able to differentiate between two groups of hydrogen-rich SLSNe, which are rarer by volume than SLSNe I. The first is that of strongly interacting SNe such as SN 2006gy (Ofek et al. 2007; Smith et al. 2007; Agnoletto et al. 2009) of which the enormous luminosity is undeniably powered by the interaction of SN ejecta with dense circumstellar medium (CSM) shells and hence usually referred to as SLSNe IIn to highlight the similarity with normal Type IIn. Whereas the second group is that of bright, broad-lined H-rich SNe labelled SLSNe II, such as SN 2008es (Gezari et al. 2009; Miller et al. 2009), which have shallow but persistent and broad Balmer lines (see Inserra et al. 2016b, for a review). They show spectroscopic evolution that is similar, in some ways, to Type II-L SNe, but the evolution happens on a longer time-scale.

The mechanisms responsible to power the luminosities of SLSNe I and II are still debated. However, the most favoured is that of a magnetar as a central engine, depositing additional energy into the SN ejecta (Kasen & Bildsten 2010; Woosley 2010; Dessart et al. 2012). The popularity of this scenario is due to its ability to reproduce a variety of observables for all the types (e.g. Inserra et al. 2013, 2016b; Nicholl et al. 2013). However, alternative scenarios such as the accretion on to a central black hole (Dexter & Kasen 2013), the interaction with a dense CSM (e.g. Chevalier & Irwin 2011) or between two massive shells (pulsational pair instability; Woosley, Blinnikov & Heger 2007) and a pair-instability explosion (e.g. Kozyreva & Blinnikov 2015) are still feasible alternatives.

Due to their intrinsic brightness, SLSNe I are emerging as high-redshift probes and might be a new class of distance indicators (Inserra & Smartt 2014; Papadopoulos et al. 2015; Scovacricchi et al. 2016). To use them with the new generation of telescopes such as the Large Synoptic Survey Telescope or *Euclid*, we need novel approaches to better understand their progenitor scenario, reveal the mechanism powering the light curve and investigate on the nature of their differences. These new approaches include analyses of large data set (e.g. Nicholl et al. 2015b), spectropolarimetric studies (Leloudas et al. 2015b; Inserra et al. 2016b,c) or devoted spectroscopic modelling of photospheric (Mazzali et al. 2016) and nebular spectroscopy (Jerkstrand et al. 2017).

The slow-evolving group of SLSNe I, of which the first to be discovered was SN 2007bi (Gal-Yam et al. 2009; Young et al. 2010), is small in number but of particular interest because the light curves decline at a rate consistent with powering by ^{56}Co during first 100–200 d after maximum. A very large amount of explosively produced ^{56}Ni is required to power the peak through ^{56}Co decay (to produce stable ^{56}Fe). With estimates in the region of 4–6 $M_{\odot}$, this led Gal-Yam et al. (2009) to propose a pair-instability explosion origin for SN 2007bi (in combination with spectral analysis) from a very massive progenitor star above $M_{\rm ZAMS} \simeq 150$ $M_{\odot}$. Hence, any new objects with similar light curve and spectra behaviour are of interest to study over long durations.

Here we present an extensive data set for LSQ14an, a slow-evolving SLSN I discovered by the La Silla QUEST (LSQ) survey and studied by the Public ESO Spectroscopic Survey for Transient Objects (PESSTO;[1] Smartt et al. 2015). To draw a meaningful comparison, we compare it with a sample of slow-evolving SLSNe I at low redshift ($z < 0.2$). There are three objects that share very similar characteristics that make up this comparison – SN 2007bi (Gal-Yam et al. 2009; Young et al. 2010), PTF12dam (Nicholl et al. 2013; Chen et al. 2015; Vreeswijk et al. 2017) and SN 2015bn (Nicholl et al. 2016a,b). These objects all have rest-frame spectra coverage up to at least 8000 Å and late-time spectroscopy and photometry up to 400 d. We will also discuss the higher redshift, and perhaps more extreme PS1-14bj (Lunnan et al. 2016). These comparisons allow us to further investigate the explosion mechanism and the progenitors of these transients, as well as the role of interaction with a CSM.

2 LSQ14AN OBSERVATIONS AND DATA REDUCTION

LSQ14an was discovered on UT 2014 January 02.3 by the LSQ survey (Baltay et al. 2013). The LSQ camera used a broad composite filter covering the SDSS *g* and *r* bands, from 4000 to 7000 Å and the pipeline initially reported a discovery magnitude of $m \sim 19.1$ mag in this filter. The object was promptly classified within 24 h by PESSTO as an SLSN roughly 50 d after peak brightness at $z \sim 0.16$ with similarities to the slow-evolving PTF12dam and SN 2007bi (Leget et al. 2014). A more careful photometric analysis and calibration of the images from the QUEST camera to SDSS *r* band resulted in an initial magnitude of $r = 18.60 \pm 0.08$ mag, as reported in Table A2 (see Section 5 for details of the photometry).

Optical spectrophotometric follow-up was obtained with the New Technology Telescope (NTT)+EFOSC2 as part of PESSTO and supplemented with other facilities. Photometry with EFOSC2 was obtained using *BVR*+*gri* filters and was augmented with observations from the Liverpool Telescope (LT)+IO:O in *gri* filters. The EFOSC2 images were reduced (trimmed, bias subtracted and flat-fielded) using the PESSTO pipeline (Smartt et al. 2015), while the LT images were reduced automatically by the LT instrument-specific pipeline. One epoch of near-infrared (NIR) imaging was obtained with the NTT and Son of Isaac instrument. These data were also reduced using the PESSTO pipeline. To remove the contribution of the host galaxy to the SN photometry (see Section 3 for data on the host), we applied a template subtraction technique (with the HOTPANTS[2] package based on the algorithm presented in Alard 2000). We used EFOSC2 *BVR* images taken on 2015 April 17 (MJD = 57129, or an estimated +460 d after peak), and the PS1 *gri* images taken before 2013 June 24 (see Section 3) as the reference templates. On the other hand, we did not use any *JHK* templates for our single epoch of observations since the contamination is of the order of a few per cent and has no significant effect on our analysis. Since instruments with different passbands were used for the follow-up of LSQ14an, we applied a passband correction (P-correction; Inserra et al. 2016b),

[1] www.pessto.org
[2] http://www.astro.washington.edu/users/becker/hotpants.html

which is similar to the S-correction (Stritzinger et al. 2002; Pignata et al. 2004), and allows photometry to be standardized to a common system, which in our case is SDSS AB mags for *gri* and Bessell Vega mags for *BVR*. This procedure takes into account the filter transmission function and the quantum efficiency of the detector, as well as the intrinsic spectrum of LSQ14an, but does *not* include the reflectance or transmission of other optical components, as this is relatively flat across the optical range (see Inserra et al. 2016b, for further details). Optical and NIR photometry are reported in Tables A2 and A3 together with the coordinates and magnitudes of the sequence stars used (see Table A4).

Optical and NIR spectra were taken during the PESSTO follow-up campaign and were supplemented with two spectra from X-Shooter on the ESO Very Large Telescope (VLT). The log of spectral observations (eight separate epochs), with resolutions and wavelength ranges, is given in Table A1. Two further spectra were taken with the VLT at later epochs of (+365 and +410 d) when the SN was in the nebular phase and are analysed in detail in Jerkstrand et al. (2017). The PESSTO spectra were reduced in standard fashion as described in Smartt et al. (2015). The X-Shooter spectra were reduced in the same manner as described for the nebular spectra in Jerkstrand et al. (2017). We used the custom-made pipeline described in Krühler et al. (2015) that takes the ESO pipeline-produced 2D spectral products (Modigliani et al. 2010) and uses optimal extraction with a Moffat profile fit. This pipeline produced flux-calibrated spectra with rebinned dispersions of 0.4 Å pixel^{-1} in the UVB+VIS arms and 0.6 Å pixel^{-1} in the NIR arm. The PESSTO spectra taken up to 2014 April are available from the public data release Spectroscopic Survey Data Release 2 (SSDR2) at ESO. Steps to retrieve the data from the ESO Science Archive Facility are available on the PESSTO website. The final EFOSC2 spectrum on 2014 August 21 will be released in the upcoming SSDR3. All spectra will also be available on WISeREP[3] (Yaron & Gal-Yam 2012).

The *Swift* satellite observed LSQ14an with the X-ray Telescope (XRT) on four epochs (PIs: Margutti and Inserra) listed in Table A5. For each XRT observation of LSQ14an, we extracted images over the 0.3–10 keV band, and all data were reduced using the HEASARC[4] software package. We measured the observed counts in each image in apertures of 5 pixel radius (11.8 arcsec), while the background in a large region (approximately 100 pixel radius), at a location free of bright X-ray sources. We then corrected this flux for the point spread function (PSF) contained within the aperture radius. *Swift* also observed another nearby, slow-evolving SLSN, namely SN 2015bn. The monitoring of this was described in Nicholl et al. (2016a,b), and analysis of the nebular spectra was presented alongside LSQ14an in Jerkstrand et al. (2017). For comparison, we retrieved the *Swift* X-ray data (five epochs were taken; PI: Margutti) and applied similar reductions and measurements as for LSQ14an. We additionally combined all the available observations in a single stacked image in order to have a deeper measurement. All measurements for the two SLSNe are listed in Table A5.

3 HOST GALAXY, LOCATION AND REDSHIFT

The host galaxy was detected in the Pan-STARRS1 3π survey (it is outside the SDSS footprint) in all five filters *grizy*$_{\rm P1}$ (see Tonry et al. 2012, for a description of the filter set). Images in each of the filters were taken from the PS1 Processing Version 2 (PS1.PV2) stacks. All the individual images that make up these stacked images were taken before MJD 56467 (2013 June 24). This is four months before the estimated peak date of late October 2013, and hence there is unlikely to be any SN flux in the images. Magnitude measurements of the host were carried out using aperture photometry with an aperture of 2 arcsec, and the zero-points were determined with 15–18 PS1 reference stars (Schlafly et al. 2012; Magnier et al. 2013) in the field resulting in the magnitudes listed in Table 1.

As discussed in Jerkstrand et al. (2017), the position of LSQ14an was measured at $\alpha = 12^{\rm h}53^{\rm m}47\overset{\rm s}{.}82$, $\delta = -29^\circ31'27\overset{''}{.}6$ (J2000) in the astrometrically calibrated EFOSC2 images (with SExtractor). In comparison, the centroid of the host galaxy, PSO J193.4492−29.5243, was measured at $\alpha = 12^{\rm h}53^{\rm m}47\overset{\rm s}{.}81$, $\delta = -29^\circ31'27\overset{''}{.}4$ (J2000). The difference between the two is 0.2 arcsec, which illustrates that LSQ14an is effectively coincident with the dwarf galaxy host (as illustrated in Fig. 1). Ultraviolet (UV) photometry of the host was obtained with the *Swift* satellite + Ultraviolet and Optical Telescope (programme ID 33205; PI: Margutti).

Table 1. LSQ14an host galaxy observed magnitudes (AB system) and properties derived from the SED and late-time spectra (see Section 3 for further information).

uvw2 (mag)	21.94 ± 0.14
uvm2 (mag)	21.72 ± 0.15
uvw1(mag)	21.44 ± 0.16
$g_{\rm P1}$(mag)	20.93 ± 0.11
$r_{\rm P1}$(mag)	20.50 ± 0.12
$i_{\rm P1}$(mag)	20.56 ± 0.10
$z_{\rm P1}$(mag)	20.42 ± 0.14
$y_{\rm P1}$(mag)	20.43 ± 0.19
Physical diameter (kpc)	3.09
Hα luminosity (erg s^{-1})	2.41×10^{41}
SFR (M$_\odot$ yr^{-1})	1.19
Stellar mass (log(M/M$_\odot$))	$8.6^{+0.2}_{-0.1}$
sSFR (Gyr^{-1})	2.98
$12 + \log$(O/H) ($T_{\rm e}$)	8.04 ± 0.08
$12 + \log$(O/H) (PP04 N2)	8.02 ± 0.03
$12 + \log$(O/H) (PP04 O3N2)	7.96 ± 0.01
log (S/O)	-1.94 ± 0.15
log (N/O) ($T_{\rm e}$)	-1.74 ± 0.18

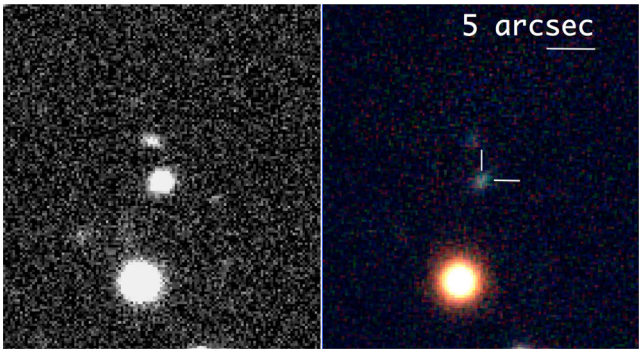

Figure 1. The left-hand panel shows the *r*-band EFOSC2 image of LSQ14an taken on 2014 January 31. The right-hand panel shows the colour composite of the host galaxy from the Pan-STARRS1 survey (constructed from $g_{\rm P1}r_{\rm P1}z_{\rm P1}$ filters). The two images are astrometrically aligned, with the centroid position of LSQ14an marked with the white cross hairs on the right. This illustrates that the SN is coincident with the dwarf galaxy host and that spectra of LSQ14an will be contaminated by the host galaxy flux since it is unresolved. The image quality of the EFOSC2 image is 0.9 arcsec FWHM and the PS1 $r_{\rm P1}$ image is 1.2 arcsec. North is up and east to the left.

[3] http://wiserep.weizmann.ac.il/home
[4] NASA High Energy Astrophysics Science Archive Research Center.

The images were co-added before aperture magnitudes were measured following the prescription of Poole et al. (2008). A 5 arcsec aperture was used to maximize the signal-to-noise ratio (S/N). The UV magnitudes were determined by averaging the measurements of MJD 56740.52 (2014 July 03) and MJD 56998.41 (2014 December 07) when the SN flux was already dimmer than that of the host. We measured $uvw2 = 21.94 \pm 0.14$, $uvm2 = 21.72 \pm 0.15$ and $uvw1 = 21.44 \pm 0.16$ mag in the AB mag system.

The host galaxy emission lines from LSQ14an are strong and conspicuously narrower than the SN emission features, and they do not evolve in our spectral series. We used Hα and other galaxy lines to refine the host redshift to $z = 0.1637 \pm 0.0001$, equivalent to a luminosity distance of $D_{\rm L} = 766$ Mpc assuming a fiducial cosmology of $H_0 = 72$ km s^{-1}, $\Omega_{\rm M} = 0.27$ and $\Omega_\lambda = 0.73$. The foreground Galactic reddening towards LSQ14an is $E_{\rm G}(B-V) = 0.07$ mag from the Schlafly & Finkbeiner (2011) dust maps. The available SN spectra do not show Na ID lines from the host galaxy; hence, we adopt a total reddening along the line of sight towards LSQ14an of $E_{\rm tot}(B-V) = 0.07$ mag.

To estimate physical diameters of the host galaxy, we assumed (galaxy observed FWHM)^2 = (observed PSF FWHM)^2 + (intrinsic galaxy FWHM)^2. The measured full width at half-maximum (FWHM) of the galaxy and the PSF were 1.65 and 1.21 arcsec, respectively (with the stellar PSF FWHM averaged over 16 reference stars in *r*-band images, located within a 2 arcmin radius of the host in the images). The angular size distance at this redshift ($D_A = 565.6$ Mpc) implies a physical diameter of the galaxy of ∼3.09 kpc.

From the VLT+X-Shooter spectrum taken on 2014 June 21 (see Table A1), we measured the observed emission line fluxes of PSO J193.4492−29.5243 (see Fig. 2, top panel). Emission line measurements were made after fitting a low-order polynomial function to the continuum and subtracting off this contribution. This continuum flux is composed of the underlying stellar population of the host and the SN flux. No significant stellar absorption was seen in the spectrum, so we did not use stellar population model subtraction method. We fitted Gaussian line profiles of those emission lines using the QUB custom-built PROCSPEC environment within IDL. We let the FWHM vary for the strong lines and fixed the FWHM for weak lines adopting the FWHM of nearby stronger, single transitions. The equivalent widths (EWs) of lines were determined after spectrum normalization. However, we caution that the normalized continuum has SN flux contamination and therefore the EW of each line is a minimum value (rather than a real line strength compared to the galaxy continuum). Uncertainties were calculated from the line profile, EW and rms of the continuum, following the equation from Gonzalez-Delgado et al. (1994). The observed flux measurement and related parameters are listed in Table A6. The lines are identified as those commonly seen in star-forming galaxies, such as Green Peas (e.g. Amorín et al. 2012) and other SLSN hosts (e.g. see Chen et al. 2015, for a comprehensive line list for the host of PTF12dam).

We used the 'direct' $T_{\rm e}$ method, following the prescription of Nicholls et al. (2013) and assuming Maxwell–Boltzmann distribution, based on the detection of [O III] λ4363 line and found $T_{\rm e}$([O III])=13 700 ± 1200 K. We can then infer a T[O II] = 13 100 ± 800 K, resulting in an oxygen abundance of 12 + log (O/H) = 8.04 ± 0.08, equivalent to 0.22 $Z_\odot$ considering a solar value of 8.69 (Asplund et al. 2009). We also checked the electron temperature at the lower ionization zone using the ratio of the nebular lines [O II] λλ7320, 7330 and thus retrieved $T_{\rm e}$([O II]) of ∼7100 K, which is much lower than the inferred T[O II]. We believe that the discrepancy is due to the low S/N of the [O II] lines with a large SN flux contamination, and hence we do not use the T[O II]. We used the open-source PYTHON code PYMCZ from Bianco et al. (2016) to alternatively calculate metallicity of the host of LSQ14an with different strong line calibrations, and we listed them as follows: 12 + log (O/H) = 8.02 ± 0.02 from the N2 method (Pettini & Pagel 2004) and 12 + log (O/H) = 7.96 ± 0.01 from the O3N2 method (Pettini & Pagel 2004). The R23 value of 0.9 is at an insensitive regime, so we do not use this scale here.

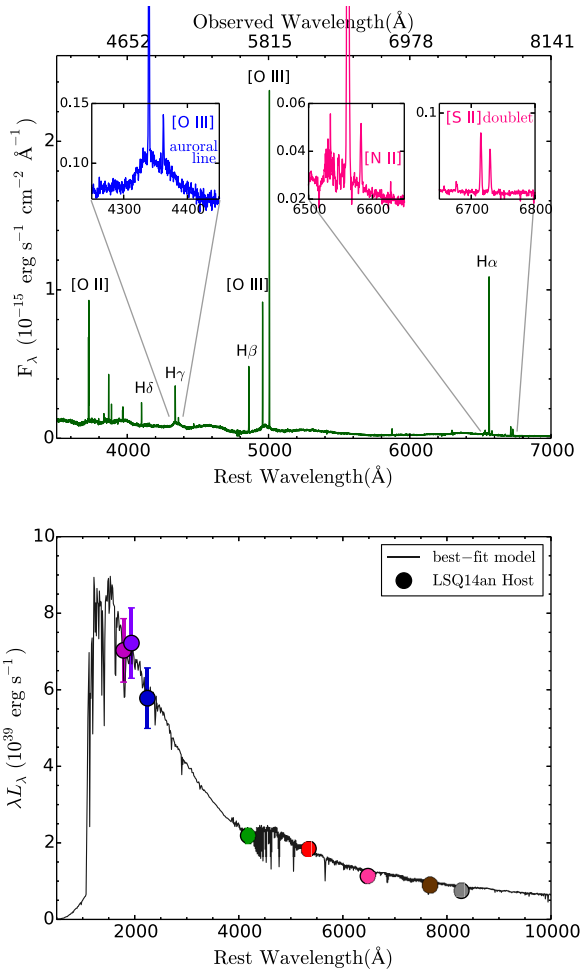

Figure 2. Top: spectrum of the host of LSQ14an taken by VLT+X-Shooter on 2014 June 21. The spectrum in the merged data from the UVB, VIS and NIR arms, corrected to rest frame. Host lines are labelled in the spectrum. Bottom: the best-fitting SED of the host of LSQ14an from MAGPHYS (da Cunha, Charlot & Elbaz 2008) shown as black line. The coloured circles show photometry of LSQ14an host in the order of the *Swift* *uvw2*, *uvm2*, *uvw1* and Pan-STARRS1 *grizy* filters.

We employed the MAGPHYS stellar population model program of da Cunha et al. (2008) to estimate the stellar mass from the observed photometry (after foreground extinction correction) of the host galaxy. MAGPHYS gives the best-fitting model spectrum ($\chi^2_{\rm red} = 0.316$) and the total stellar mass of the hosts (see Fig. 2). The median and the 1σ range of the stellar mass of LSQ14an host are $4.0^{+2.5}_{-1.1} \times 10^8$ $M_\odot$, which is consistent with the measurements of Schulze et al. (2016) for the same host, and that retrieved in SLSN hosts (e.g. Lunnan et al. 2014; Leloudas et al. 2015a; Perley et al. 2016).

We converted the Hα luminosity of 2.41×10^{41} erg s^{-1} to calculate the star formation rate (SFR) using the conversion of Kennicutt (1998) and a Chabrier initial mass function (IMF).[5] We found an SFR of LSQ14an host SFR $= 1.19$ M$_{\odot}$ yr^{-1}, which is higher than the average, but still consistent with other slow-evolving SLSNe I (e.g. Chen et al. 2015; Leloudas et al. 2015a). In this case, our estimate is somewhat lower than that reported by Schulze et al. (2016). Considering the stellar mass previously evaluated, we determined the specific SFR (sSFR) of 2.98 Gyr^{-1} for the host of LSQ14an. A summary of LSQ14an host galaxy properties is reported in Table 1.

4 SPECTRA

The first spectra taken of LSQ14an by PESSTO (Leget et al. 2014) already suggested an epoch well after maximum brightness. The absence of the characteristic broad O II absorption lines observed in SLSNe, at and before the peak epoch, together with a temperature of ∼8000 K – derived from the blackbody fit to the continuum of our spectra – confirm the initial classification phase. In order to secure the phase with more precision and estimate the date of the peak of the light curve, we compared our classification spectrum with other slow-evolving SLSNe I. As highlighted in the top panel of Fig. 3, the LSQ14an spectrum taken on the 2014 January 2 is very similar to those of the three other objects with broad light curves: SN 2007bi, PTF12dam and SN 2015bn at 50 to 60 d after peak.

At this phase, the emission lines that are developing and becoming pronounced are similar to those that have quantitatively been identified and modelled by Jerkstrand et al. (2017). The Mg I] λ4571 line is strong, and this usually begins to appear about ∼35 d post-peak (Inserra et al. 2013; Nicholl et al. 2016a). The region between 5000 and 5800 Å shows a broad emission feature that is likely a blend of Mg I λ5180, [Fe II] λ5250 and [O I] λ5577. There is a distinct lack of absorption that could be attributed to Si II λ6355, and the forbidden doublet of [O I] λλ6300, 6363 is beginning to emerge in emission (see Fig. 4 for line identification). Finally, the [Ca II] λλ7291, 7323 line strength and the EW of O I λ7774 both support an epoch of the spectrum of +50–55 d after maximum in the rest frame.[6] As a consequence, assuming a phase of +55 d for the first spectrum, we estimate the peak epoch to have been MJD 56596.3 ± 5.0 (around 2013 October 31). This date is consistent with our analysis of the light-curve evolution (see Section 5).

For comparison, we also showed the earliest PESSTO spectrum of LSQ14an together with faster evolving SLSNe (bottom panel of Fig. 3). SN 2011ke and SN 2012il decline much faster than the other three comparison objects and are similar to SN 2010gx in their overall evolution (see Inserra et al. 2013, for a discussion of these two objects). CSS121015 is a peculiar SLSN I that shows weak signs of interaction with a hydrogen CSM that fade with time, displaying broad lines similar to those of SLSNe I (Benetti et al. 2014). In this comparison, the noticeable differences are that the Mg I] line has a larger EW (a factor of 2 higher in LSQ14an than the others), and the fast-evolving SLSNe do not show the forbidden [O I] and [Ca II] at this phase. In truth, a clear detection of [Ca II] has only been recently reported for a fast-evolving SLSN (at +151 d from maximum in Gaia16apd, Kangas et al. 2016, an SLSN that shows a late photometric behaviour intermediate between the fast- and slow-evolving events), but see Section 4.2 for a more detailed analysis of the elements contributing to the feature. The continuum of LSQ14an and the other slow-evolving objects above are also significantly bluer than the fast-evolving and stay blue for longer (more than a factor of 3 in time) as already noted for SN 2015bn by Nicholl et al. (2016a). The prominent emission feature at 5200–5600 Å has a markedly different profile shape in LSQ14an – sharper with a peak consistent with it being a blend of Mg I λ5180 and [Fe II] λ5250. This profile is similar to that marking the beginning of the pseudo-continuum, dominated by Fe lines, in interacting SNe such as SNe 2005gl and 2012ca (Gal-Yam et al. 2007; Inserra et al. 2016a) but in the SLSN case the feature is 200 Å bluer and not as sharp as in the interacting transients.

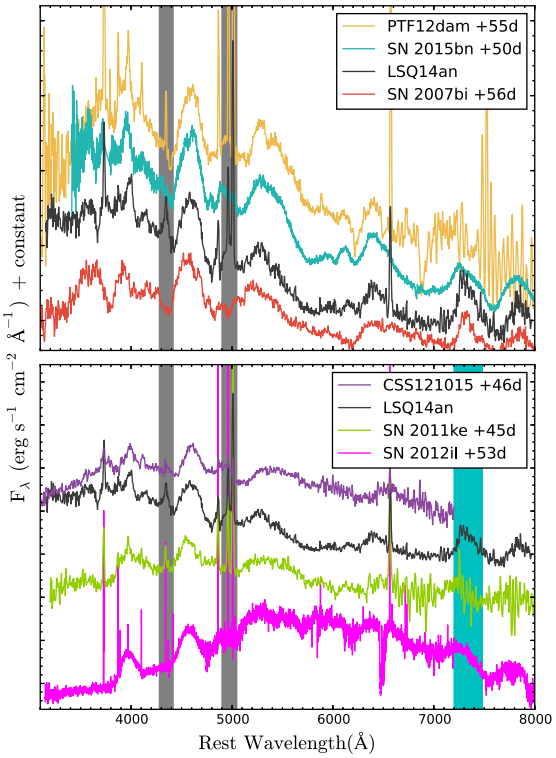

Figure 3. Top: comparison of LSQ14an classification spectrum with those of other slow-evolving SLSNe I (SN 2007bi, PTF12dam, SN 2015bn; Gal-Yam et al. 2009; Young et al. 2010; Nicholl et al. 2013, 2016a) around 50 d post-maximum suggesting that LSQ14an was discovered at ∼55 d from maximum light. Bottom: same LSQ14an spectrum of the top panel compared with fast-evolving SLSNe I (SN 2011ke, SN 2012il and CSS121015; Inserra et al. 2013; Benetti et al. 2014) in order to highlight the differences. The grey areas identify the [O III] lines observed in emission in LSQ14an spectra, while the cyan in the bottom panel identifies the region of the [Ca II] λλ7291, 7323.

In Fig. 4, we show the optical spectroscopic evolution of LSQ14an with nine spectra taken from +55 to +253 d after the estimated peak epoch. At all epochs, the spectra are 'pseudo-nebular', showing permitted, semi-forbidden and forbidden lines. However, it is remarkable that the lines that are unambiguously identified in Jerkstrand et al. (2017) through modelling the nebular phase spectra at +300–400 d are already visible and prominent at +50 d (cf. Fig. 5). We note that the epoch of the first spectrum is supported by the previous spectroscopic comparison of Fig. 3 and also by LSQ14an photometric evolution (cf. Section 5). The strongest emission line features are almost all the same in these spectra that

[5] The tool employed to evaluate the SFR uses a Chabier IMF, while Kennicutt (1998) a Salpeter IMF. We took that into account dividing the SFR by a factor of 1.6.

[6] All the phases are reported in rest frame unless otherwise stated.

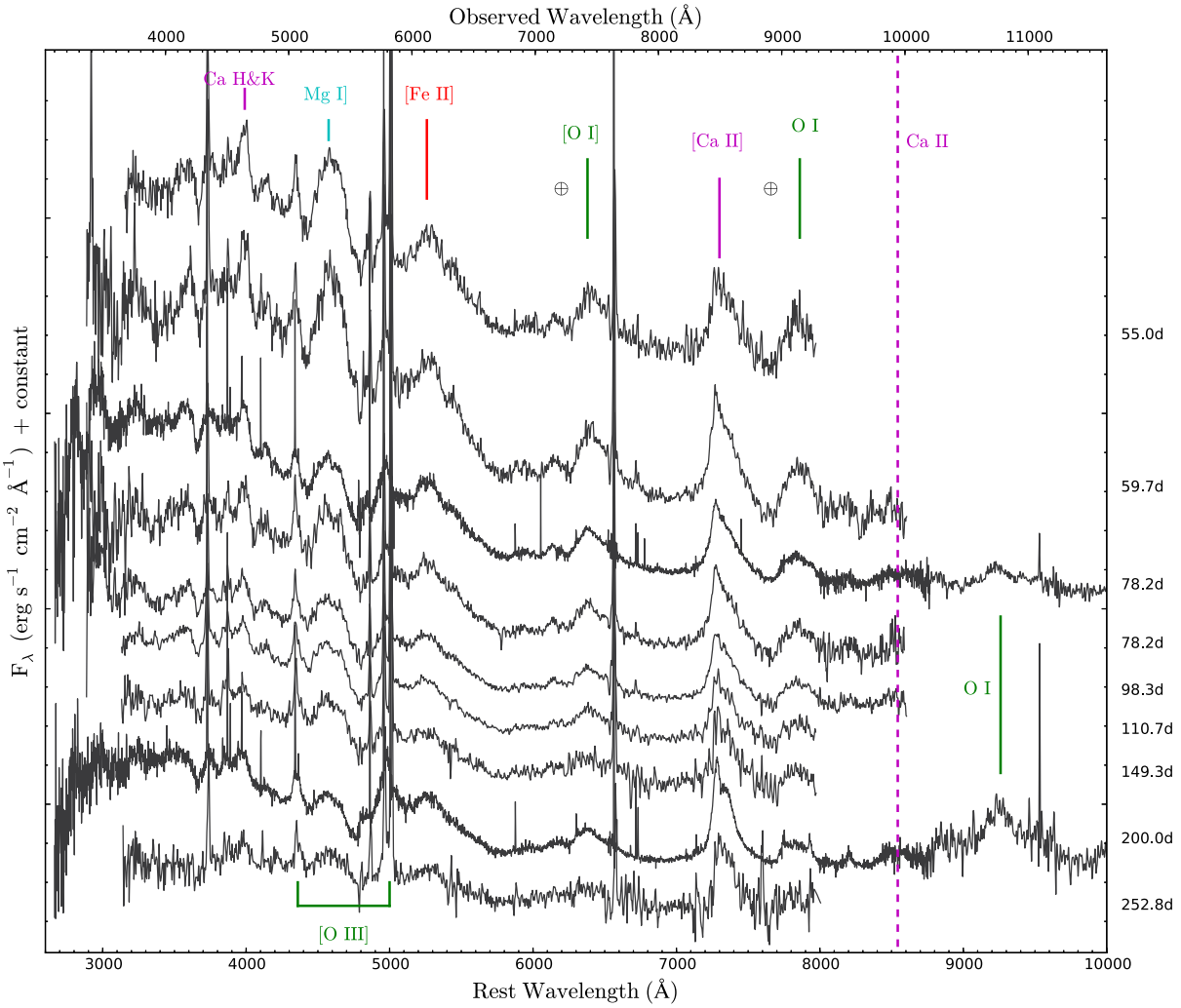

Figure 4. Spectral evolution of LSQ14an. The phase of each spectra is relative to the assumed peak epoch. The ⊕ symbol marks the positions of the strongest telluric absorptions. The most prominent features are labelled, together with the position (dashed magenta line) of the NIR Ca II, which is not observed.

are separated by a long time interval up to a year (see Fig. 5 in this paper and fig. 7 of Jerkstrand et al. 2017). The strong blue continuum is a feature of both LSQ14an and SN 2015bn even after subtraction of the blue host galaxy. A similar behaviour is also shown by SN 2015bn on an almost equivalent time baseline of LSQ14an (Fig. 5). The strongest emission lines identified at late time are already in the +72 d spectrum (and in any spectrum after ∼50 d post-peak; see Nicholl et al. 2016a). The only small difference is the [O I] λλ6300, 6364 that appears later in SN 2015bn (Jerkstrand et al. 2017). We note that the continuum flux of the host galaxy becomes comparable to the SN at +150 d and later; therefore, the last two spectra at +200 and +252 d will contain host galaxy flux.

The NIR coverage of X-Shooter at +78 and +200 d allows the identification of the line at 9200 Å as O I λ9263. This line was identified as O I in the modelling of the +315 d spectrum of SN 2015bn and the +365 d spectrum of LSQ14an by Jerkstrand et al. (2017). This is a recombination line ($2s^2 2p^3 (^4S^\circ) 3p$), and we measure an FWHM of $v \sim 8000$ km s^{-1} in the +200 d spectrum. The O I λ7774 is another recombination line that decays from the lower state of the O I λ9263 transition. As expected, the two lines have the same velocity.

We also measured the FWHM velocity of the [O I] and [Ca II], which are usually the strongest forbidden lines in nebular spectra of SNe. They display an almost constant velocity with average $v \sim 7500$ km s^{-1} for [O I] and $v \sim 7400$ km s^{-1} for [Ca II]. The calcium line, clearly not Gaussian, is noticeably asymmetric (see Section 4.2) throughout the evolution and is much stronger than [O I]. The feature could be a blend of [O II] λλ7320, 7330 and [Ca II] λ7291,7323. A more detailed discussion of this and the implications for the explosion mechanism are presented in Jerkstrand et al. (2017). However, we already notice that lines coming from the same elements show different velocities and how semi-forbidden and forbidden lines are observed earlier and at higher temperatures than normal stripped envelope SNe.

What is surprising is the absence of the Ca II NIR triplet λλ8498, 8542, 8662 up to 200 d (see Fig. 4), whereas it is present at +365 d in Jerkstrand et al. (2017). Since it requires high temperatures, this feature is usually seen quite early and disappears after 100 d. In contrast, in LSQ14an the evolution is the opposite and in some extent similar to that of SN 2015bn where the NIR Ca grows in strength from 100 d to more than 300 d (Nicholl et al. 2016b; Jerkstrand et al. 2017). The two X-Shooter spectra have a

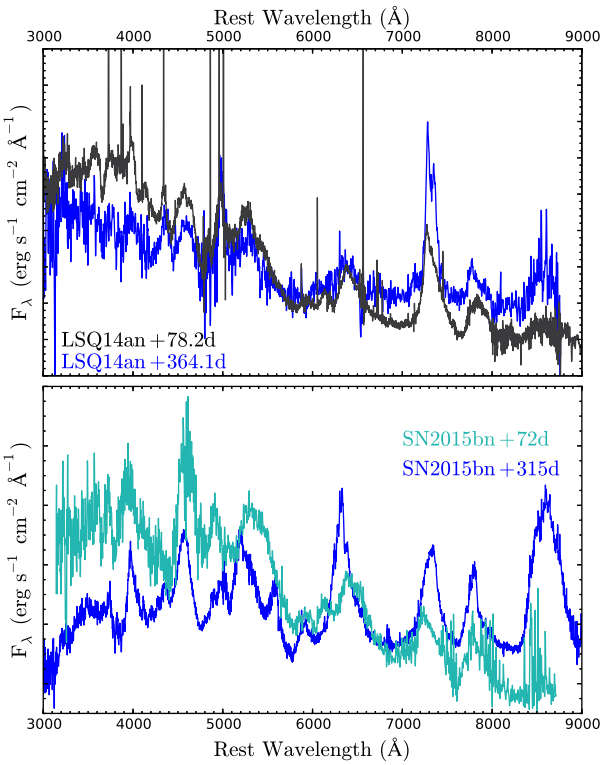

Figure 5. Top: LSQ14an at +78 d (black) and +364 d (blue, after subtraction of the galaxy model, and removal of host galaxy lines). Note that the +364 d spectrum (Jerkstrand et al. 2017) has been scaled by 2.3 to match the earlier one. The lines have not changed in almost a year. The same is true if the +50 and +409 d (Jerkstrand et al. 2017) spectra are compared. Bottom: similar comparison of before but for SN 2015bn (Nicholl et al. 2016a; Jerkstrand et al. 2017).

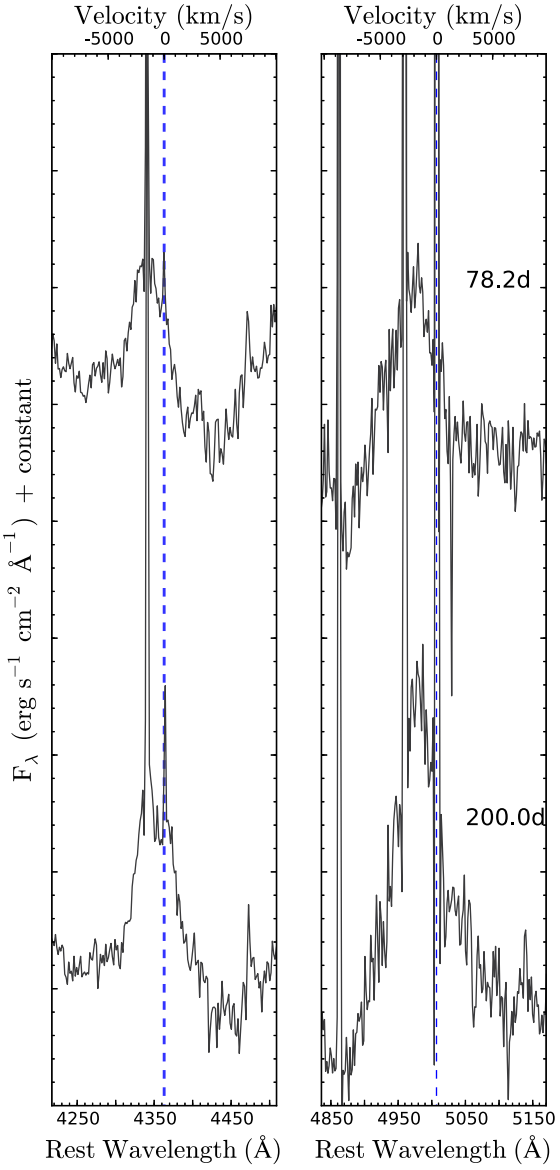

Figure 6. Left: LSQ14an [O III] λ4363 evolution from the two X-Shooter spectra at +78.2 and + 200.0 d. Right: LSQ14an [O III] λλ4950, 5007 evolution. The zero velocity is set at 5007 Å, since that is the strongest component of the [O III] doublet. The vertical dashed blue lines denote the centroids of the lines. H γ (right-hand panel) and H δ (left-hand panel) are also visible.

coverage out to 2.0 μm in the rest frame, but they are featureless beyond 1.0 μm and display no strong and identifiable emission lines.

The narrowest emission lines that are lines observable throughout the spectroscopic evolution, are the Balmer, [O II] and [O III] lines due to the host galaxy. They have a constant velocity of $v = 150 \pm 20$ km s^{-1} (measured from the two X-Shooter spectra) comparable with those of the host galaxies of SLSNe in previous studies (e.g. Leloudas et al. 2015a).

4.1 [O III] λ4363 and λλ4959, 5007 lines

A peculiarity shown by the spectroscopic evolution of LSQ14an is the presence of a broad component of [O III] λ4363 and λλ4959, 5007 (see Fig. 6). In the first two PESSTO spectra with EFOSC2, these oxygen lines are prominent but the resolution of the Grism#13 prevented easy identification of emission broader than the host galaxy lines (see Fig. 6). The first X-Shooter spectrum taken at +78 d shows that [O III] λ4363 and λλ4959, 5007 have a broad component arising in the SN ejecta. The existence and origin of these lines as broad [O III] was first pointed out by Lunnan et al. (2016, for PS1-14bj that is a very slow evolving SLSN) and they have been analysed in detail in Jerkstrand et al. (2017) in the later nebula spectra.

The average velocities of the components, as measured from the two X-Shooter spectra, are $v_{\lambda 4363} \sim 3200$ km s^{-1} and $v_{\lambda\lambda 4959,\,5007} \sim 3500$ km s^{-1} (see also Fig. 6). Although these broad lines are severely blended with the galaxy emission lines in the lower resolution PESSTO spectra, we measure no velocity evolution in the FWHM of the features over the whole period (similarly to the other lines discussed in Section 4). The velocities of [O III] we measure from the X-Shooter spectra are a factor of 2–3 less than those of the [O I] forbidden lines and the O I recombination lines. Even if we assume a low-mass, dilute oxygen region, allowing a higher energy deposition than the other slow-evolving SLSNe (Jerkstrand et al. 2017), this would not take into account their intrinsic different velocities, which could be explained with multiple emitting regions. Something similar was suggested in the case of SN 2015bn but for different oxygen lines (Nicholl et al. 2016b).

The measured ratio for these collisionally excited lines in the optically thin limit can provide some information about the electron density of the emitting region where those are formed,

$$\frac{f_{\lambda\lambda 4959,5007}}{f_{\lambda 4363}} = \frac{7.90\exp(3.29\times10^4/T)}{1+(4.50\times10^{-4}\times n_e/T^{\frac{1}{2}})}, \quad (1)$$

from Osterbrock & Ferland (2006), where T is the temperature and n_e is the electron density of the medium. We measured $f_{\lambda\lambda 4959,\,5007}/f_{\lambda 4363} = 1.8$ from our X-Shooter spectra on an average of two measurements with a Gaussian fit. The ratio is consistent with that reported by Lunnan et al. (2016) for PS1-14bj (<3) and hence less than what is typically observed in gaseous nebulae (Osterbrock & Ferland 2006) and nebular Type IIn (e.g. SN 1995N; Fransson et al. 2002). We initially assumed the ejecta temperature ($T \sim$8000 K) and found $n_e = 6.2\times10^7$ cm^{-3} for the emitting region of the [O III] lines. If we increase the assumed temperature to $T = 20\,000$ K, the density decreases to $n_e = 8.0\times10^6$ cm^{-3}. By comparison, the [O I] λλ6300, 6363 arising from the inner region of the ejecta has $n_e \sim 10^9$ cm^{-3} (as measured for late spectra of LSQ14an, ∼200 d later, by Jerkstrand et al. 2017, and having taken into account that density evolves as t^{-3}). These lines are mainly collisionally excited with thermal ions at all times, as they are close to the ground state (see Jerkstrand et al. 2017, for a more in-depth analysis).

Although [O III] and [O I] can come from the same physical region, the different densities (n_e([O III]) <n_e([O I]), velocities (v([O III]) < v([O I])) and the absence of a comparable strong [O II] λ7300 would suggest that these lines are formed in two different regions (see Section 8 for the interpretation).

In the magnetar scenario, the [O III] lines could come from an oxygen-rich ejecta layer that is ionized from the X-ray energy coming from the inner engine. This would be very similar to the scenario of a pulsar wind nebula expanding in an H- and He-free SN gas, for which the second strongest lines predicted are [O III] λ4959, 5007 (Chevalier & Fransson 1992). On the other hand, the strongest lines observable in an H-free pulsar wind nebula should be those of [S III] λλ9069, 9532.[7] These are not observed in our NIR spectra, suggesting that it may not be the X-ray heating from the magnetar that causes the presence of the [O III] lines.

As shown in Fig. 6, we also note that the peak of the [O III] λ4363 is blueshifted by ∼1400 km s^{-1} compared to the rest frame of the SN and the centroid of the [O I] lines (see Table 2 for a comparison between the velocities of the oxygen lines). Similarly, the [O III] λλ4959, 5007 lines have a centroid that appears shifted of ∼1400 km s^{-1}. These lines and shifts are clear in the high-resolution X-Shooter spectra, but are not easily discerned in the lower resolution EFOSC2 spectra.

4.2 Forbidden lines around 7300 Å

Explosively produced calcium would likely come from an O-burning zone rather than a C-burning zone, where the [O I] λλ6300, 6363 lines would form. In slow-evolving SLSNe, [Ca II] λλ7291, 7323 has been observed in emission from surprisingly early stage: about 50–70 d from maximum (e.g. SNe 2007bi, 2015bn; Gal-Yam et al. 2009; Young et al. 2010; Nicholl et al. 2016a). We see similar behaviour from LSQ14an. [Ca II] appears almost at the same phase

[7] We note that if hydrogen is also present in the nebula, [O III] λ5007 and [S II] λ6723 are stronger than [S III] (Kirshner et al. 1989). However, in our case also [S II] is not observed.

Table 2. Breakdown of the oxygen and calcium lines analysis from our X-Shooter spectra of LSQ14an (see Sections 4.1 and 4.2).

Phase (d)	+78.2	+200.0
	[O I] λλ6300, 6363	
Shift (km s^{-1})	–	–
v (FWHM, km s^{-1})	7500	7500
n_e (cm^{-3}) [a]	∼10^9	∼10^9
	[O III] λ4363	
Shift (km s^{-1})[b]	−1400	−1400
v (FWHM, km s^{-1})	3200	3200
n_e (cm^{-3})	∼10^7	∼10^7
	[O III] λλ4959, 5007	
Shift (km s^{-1})[b]	−1400	−1400
v (FWHM, km s^{-1})	3500	3500
n_e (cm^{-3})	∼10^7	∼10^7
	[Ca II] λλ7291, 7323	
Shift (km s^{-1})[b]	−1300	0
v (FWHM, km s^{-1})	7400	7400
n_e (cm^{-3})[a]	>10^9	>10^9
	[O II] λλ7320, 7330 +[Ca II] [c]	
Shift (km s^{-1})[b]	−1900/−1700	−1400/0
v (FWHM, km s^{-1})	1700/2800	1700/2800
n_e (cm^{-3})[a]	∼10^9/>10^9	∼10^9/>10^9

Notes. [a]Data derived from the estimates reported in Jerkstrand et al. (2017).
[b]w.r.t. the centroid of the line or main doublet.
[c]Left values are related to [O II], while the right to [Ca II].

in normal stripped envelope SNe (after 60–70 d, e.g. SNe 1994I, 2007gr; Filippenko et al. 1995; Hunter et al. 2009) and later in broad-lined SNe (after 100 d, e.g. SN 1998bw; Patat et al. 2001), which however have less massive ejecta than the slow-evolving SLSNe. Also in fast-evolving SLSNe, it appears at least after 100 d from peak (Kangas et al. 2016). Hence, in SLSNe, where it is detected, it seems to appear earlier than expected.

The [Ca II] profile shows a component that has a peak at a velocity of −1300 km s^{-1} with respect to rest-frame [Ca II]. Although we are somewhat limited by the EFOSC2 resolution, the blueshifted peak is visible in all spectra from +55 to +253 d (see Fig. 7). The X-Shooter spectra show the line profile well resolved and indicate that this is not a simple blueshifting of the peak of [Ca II]. The three most likely explanations are either asymmetry in the [Ca II] emitting region, a second [Ca II] emitting region that is at a different velocity or another ionic component. Fig. 7 shows a double Gaussian fit to the broad [Ca II] in the second epoch (FWHM = 7400 km s^{-1}) with the blue peak visible. If this is [Ca II], then the blueshift of −1300 km s^{-1} is similar to that observed in the [O III] lines. Therefore, the region that is producing the [O III] lines may also be emitting [Ca II].

There is an iron line, [Fe II] λ7155, but this transition is 120 Å too far blue and the X-Shooter profile would not support that identification. Furthermore, we would also have expected to observe [Fe II] λ1.257 μm with a similar strength, but the spectra at that wavelength are featureless. Jerkstrand et al. (2017) showed that the strength of the overall emission feature of [Ca II] is much stronger in LSQ14an than in the other two comparator objects (SN 2015bn and SN 2007bi). Their models at +365 and +410 d indicate that there is likely a significant contribution from [O II] λλ7320, 7330. If the blue peak is indeed dominated by [O II] λλ7320, 7330, then it is blueshifted by −1920 km s^{-1} and has a width of around 1700 km s^{-1} (from a blended two Gaussian fit as evaluated by the 200 d epoch). It is possible that this is [O II] from the same physical region that is producing the narrow [O III] lines, since the blueshift is similar.

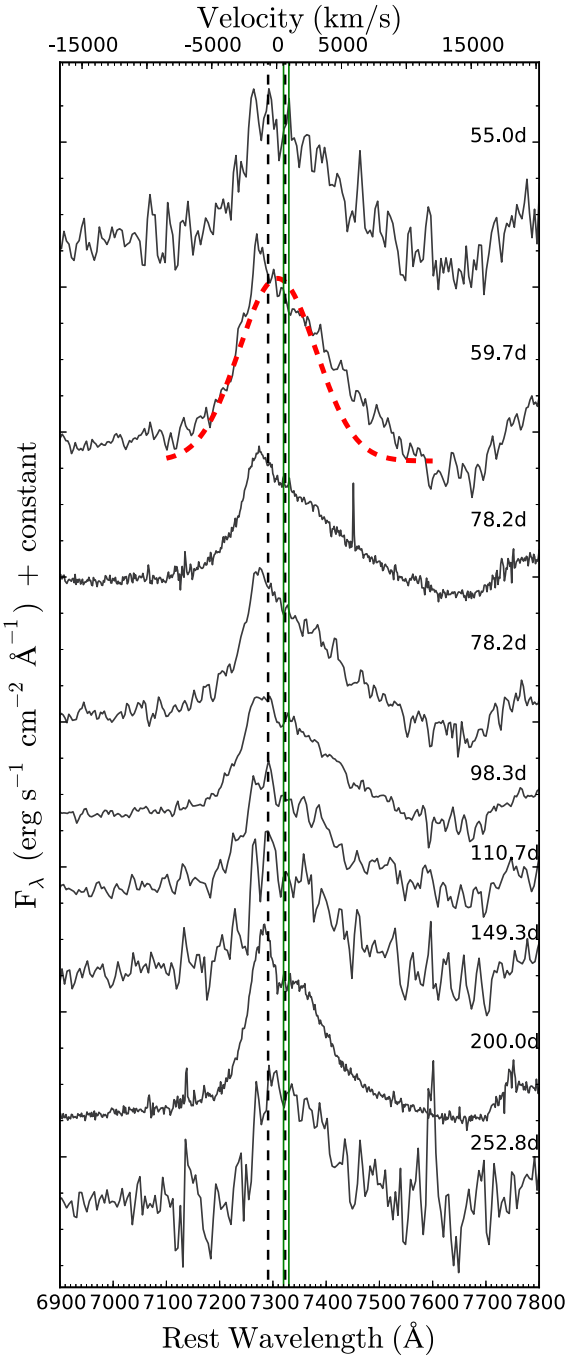

Figure 7. LSQ14an [Ca II]+[O II] evolution from the first epoch at +55.0 d to the last at +252.8 d. A double Gaussian fit (red dashed line) to [Ca II] is shown for the +59.7 d epoch to highlight the skewed shape of the profile. The two vertical black dashed lines denote λλ7291, 7323 at rest frame, while the solid green mark [O II] λλ7320, 7330. The zero velocity is set at the centroid of the [Ca II] doublet. Phase with respect to the maximum is also shown.

The velocity width of the line is lower than that estimated for [O III] (of the order of 2900 km s^{-1}), but the blending of both these lines with the broad [Ca II] component means that both estimates are uncertain. It is certainly clear that both are narrower than the widths of main components of [Ca II] and [O I], which are of the order of 7000–8000 km s^{-1} and that the feature exhibits a blueshift.

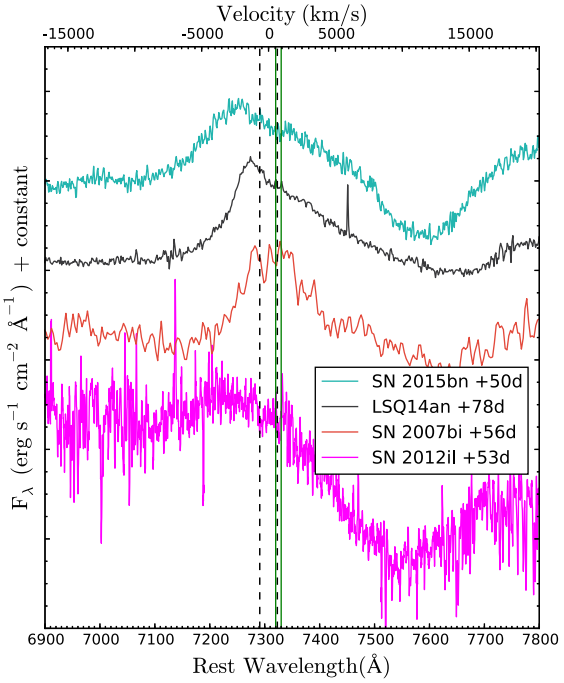

Figure 8. Blueshifted [Ca II]+[O II] profile of LSQ14an compared to the same line of other two slow-evolving SLSNe at similar epoch. The two vertical black dashed lines denote λλ7291, 7323 at rest frame, while the solid green mark [O II] λλ 7320, 7330.

Surprisingly, LSQ14an is not the only slow-evolving SLSNe I showing this profile. As highlighted in Fig. 8, SN 2015bn[8] shows a similar blueshifted peak to that of LSQ14an, whereas that of SN 2007bi is centred at the rest wavelength. In PTF12dam, despite the low S/N of the spectra at that wavelength region, [Ca II] also appears to be centred at the rest wavelength (see extended data in fig. 3 in Nicholl et al. 2013). Therefore, we can conclude that the blueshifted feature associated with [Ca II] λλ7291, 7323 is not a unique feature of LSQ14an but is also not ubiquitous in all slow-evolving SLSNe I.

A blueshifted emission from [Ca II] is not uncommon in core-collapse SNe (CC-SNe) interacting with a CSM at late times. Type II SNe 1998S, 2007od (Pozzo et al. 2004; Inserra et al. 2011) showed a similar blueshifted [Ca II] profile, as well as Type Ib/c (e.g. Taubenberger et al. 2009; Milisavljevic et al. 2010). This is usually interpreted as a consequence of dust formation in ejecta, which causes the dimming of the red wings of line profiles due to the attenuation of the emission originating in the receding layers, or residual line opacity especially for stripped envelope SNe, as also shown by models (see Jerkstrand et al. 2015). However, in the case of LSQ14an, only [Ca II]+[O II] and [O III] show a blueshifted peak and only [Ca II]+[O II] shows a clearly skewed profile. If the explanation were dust, then it would suggest that the dust distribution is not homogeneous and most likely in clumps. Hence, we favour the component being either narrow [O II] arising from the same region as the [O III] lines (see Table 2), another component of [Ca II] also located physically with the narrow [O III] emitting region or an effect of the residual line opacity. See Section 8 for more discussion and interpretation.

[8] We chose an earlier spectrum of SN 2015bn, with respect to that of LSQ14an, due to its high S/N. However, the skewed [Ca II] is also observable later than 50 d (see Nicholl et al. 2016a).

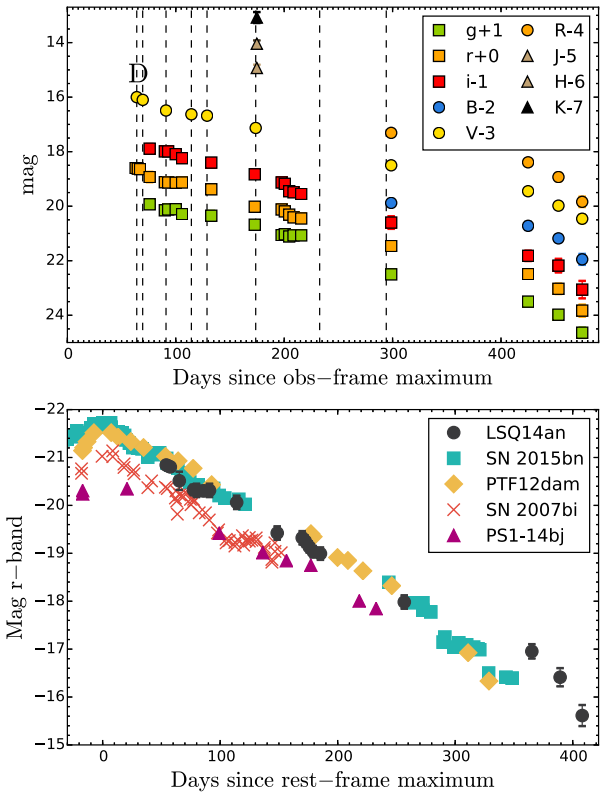

Figure 9. Top: *griBVRJHK* light curves of LSQ14an in the observer frame with respect to the assumed maximum. The epochs of spectroscopy are marked with black dashed lines, while the discovery with the letter 'D'. Bottom: comparison of the *r*-band magnitude of well-sampled slow-evolving SLSNe.

5 LIGHT AND BOLOMETRIC CURVES

5.1 Light curves

The LSQ14an light curve shows a decline in all the available bands since the discovery epoch. This confirms that the SN was discovered past peak. However, the decline rate is not uniform and the uncertainty in the photometric measurements is small enough to detect clear changes in the decline. In the *r* band, we observe a 1.8 mag 100 d^{-1} decline (2.1 mag 100 d^{-1} in rest frame) until 91 d past the rest-frame assumed peak, followed by a slower decrease of 1.2 mag 100 d^{-1} (1.4 mag 100 d^{-1} in rest frame) from 114 to 257 d and a faster decrease of 2.7 mag 100 d^{-1} (3.1 mag 100 d^{-1} in rest frame) in the last phase from 365 to 408 d. All declines are more rapid than that of ^{56}Co to ^{56}Fe, which should be at ∼1.1 mag 100 d^{-1} in the case of full trapping (Wheeler & Benetti 2000). In the bottom panel of Fig. 9, we show LSQ14an *r*-band absolute light curve compared with those of four slow-evolving SLSNe with data during the same phase. All five are similar, with the resemblance between LSQ14an, SN 2015bn and PTF12dam being particularly close. This suggests that our assumed peak epoch from the spectra comparison should be correct within the uncertainties above stated. Previously, SN 2007bi has been assumed or proposed to be a unique object that requires a physical interpretation as a pair-instability SN (PISN; Gal-Yam et al. 2009), but it is clear that there is a class of these slow-evolving SLSNe (as initially proposed by Gal-Yam 2012), which LSQ14an (and the others) is part.

5.2 Luminosity, temperature and radius

Our LSQ14an imaging data set lacks UV coverage and has only one epoch of NIR coverage. Hence, only an optical pseudo-bolometric can be built (see Inserra et al. 2016b, for further details in the construction of the bolometric light curve). Applying the *K*-correction,[9] fitting the available spectral energy distribution (SED) and integrating the flux from 1500 to 25 000 Å should provide a good approximation to the full bolometric (see Inserra et al. 2013, 2016a). Pseudo- and total bolometric light curves are shown in the top panel of Fig. 10, comparing the bolometric light curve of LSQ14an with those of other slow-evolving SLSNe I, namely SN 2007bi, PTF12dam and SN 2015bn. They are all very similar, with decline rates from peak to 150 d that match the radioactive decay of ^{56}Co to ^{56}Fe. After 150 d, all of them deviate from the ^{56}Co rate, as already noted in the case of SN 2015bn by Nicholl et al. (2016b). LSQ14an is the less noticeable in this behaviour, possibly due to the sparse sampling in that phase combined with the light-curve oscillations (see Section 6). If they were mostly powered by ^{56}Ni, then they cannot be fully trapped. This argues strongly against them being pair-instability explosions, since the massive ejecta required for this explosion mechanism inherently implies full trapping up to 500 d after maximum light (Jerkstrand, Smartt & Heger 2016). Hence, while at first sight the approximate match to ^{56}Co is appealing to invoke nickel-powered explosions, it quantitatively does not fit with massive pair-instability explosions. We also see some evidence that after 250–300 d, there may be a steepening in the decline slope in all four. The decline at times after 300 d is roughly consistent with a power law of index $\alpha = 5$ ($L \sim t^{-5}$), typical of an adiabatic expansion (a.k.a. Sedov–Taylor phase), which is unexpected at this phase (see Section 8).

The blackbody fit to the photometry delivers information about the temperature and radius evolution. We also used a blackbody fit on our spectra in order to increase the available measurements. We then compared our results with the well-sampled PTF12dam (Chen et al. 2015; Vreeswijk et al. 2017) and SN 2015bn (Nicholl et al. 2016a,b). LSQ14an shows an overall steady temperature of 8000 K, which is slightly higher than that measured in SN 2015bn and PTF12dam but still consistent within the errors.

The evolution of the blackbody radius of LSQ14an shows an overall similar behaviour to that of PTF12dam and to SN 2015bn up to 150 d. After 150 d, it remains roughly constant until the end of our data set in a similar fashion to that of PTF12dam, while SN 2015bn steadily decreases. A small increase of the radius is noticeable from ∼60 to ∼75 d, which corresponds to the first of the two possible fluctuations observed in LSQ14an light curve. Such behaviour was also observed for the undulations in SN 2015bn (Nicholl et al. 2016a).

6 LIGHT-CURVE UNDULATIONS IN HYDROGEN-POOR SLOW-EVOLVING SLSNE I

All the individual LSQ14an light curves show some low-level evidence of undulations. To explore this further, we fitted a first-order polynomial to the bolometric light curve. The choice of using the bolometric allows us to avoid an analysis dominated by *K*-correction or line evolution within a particular passband. We chose to focus from 50 to almost 250 d excluding data after 250 d due to sparse sampling. The choice of a linear function to fit is due to the fact that

[9] In this paper, all the absolute magnitudes have been *K*-corrected with the SNAKE code (Inserra et al. 2016b).

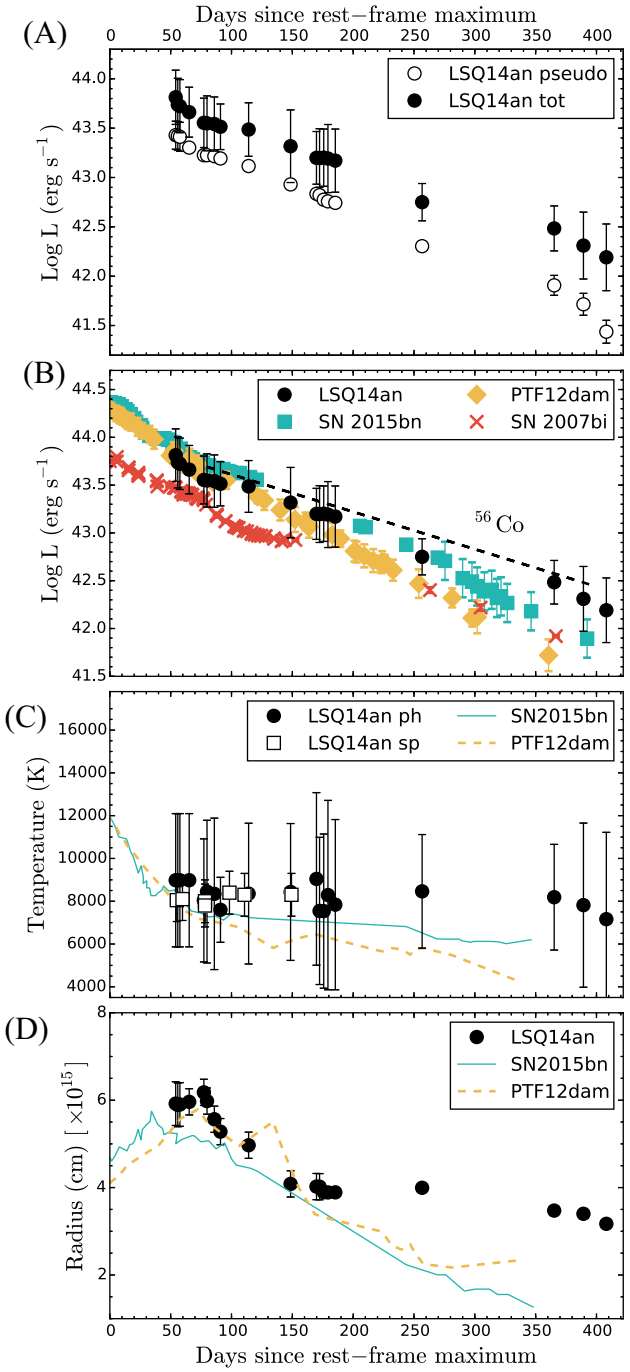

Figure 10. Panel A: bolometric light curve of LSQ14an obtained by integrating the flux over the optical band (open circles) and from UV to NIR (black filled circles). Panel B: bolometric light curve of LSQ14an compared with those of SN 2007bi, PTF12dam and SN 2015bn. The ^{56}Co-to-^{56}Fe decay slope is shown as a dashed black line. See the text for further information. Panel C: temperature evolution of best-fitting blackbody models evaluated for photometry (black circles) and spectroscopy (open squares) compared to that of the well-observed SN 2015bn (cyan solid line) and PTF12dam (orange dashed line). Panel D: evolution of blackbody radius (black circles), compared to that of the same SLSNe of panel C.

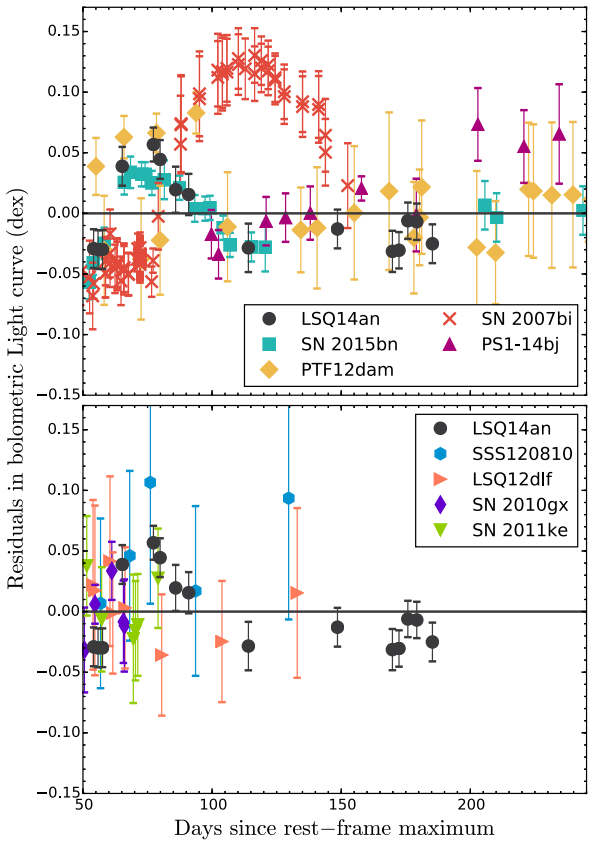

Figure 11. Top: residuals, after subtracting fits to the declining bolometric light curve, showing undulations over the selected phase in the case of slow-evolving SLSNe. Bottom: LSQ14an residuals compared with those of four fast-evolving SLSNe, which do not show any appreciable fluctuations, with the possible exception of SSS120810.

slow-evolving SLSN I light curves are usually well reproduced by models having a uniform, steady decline over the analysed baseline. We then subtracted the fit from the light curve over that time-scale. The residuals are shown in the bottom panel of Fig. 11.

The residuals appear to have at least one clear fluctuation pattern from 50 to 200 d in rest frame. At 75 d, we observe a fluctuation of 0.06 dex from the linear fit. Another less distinct oscillation (0.04 dex) is visible around 170 d. Nevertheless, there is a residual pattern that oscillates across the linear decline fit with an amplitude that appears larger than the errors on the flux measurements.

We then compared the LSQ14an residual analysis with those of our selected slow-evolving SLSN I sample. The phase analysed here is after that of the 'knee' observed in SN 2015bn (Nicholl et al. 2016a). We also observe a small fluctuation from 75 until 120 d in the SN 2015bn data, similar to that of LSQ14an but with lower amplitude (0.02–0.03 dex). None the less, our estimated errors are smaller than the observed amplitude for this SN too. PTF12dam may also have some undulations present, but in this case the amplitude is comparable to or less than the errors. Fluctuations are also observed for PS1-14bj, which shows a 0.03 dex fluctuation at around 100 d and a more noticeable one (0.07 dex) around 220 d. For all objects, the undulations are small, with an average of 0.05 dex, but they are generally greater than the photometric errors (0.01–0.03 dex depending on the phase and distance of the object). On the other hand, SN 2007bi shows stronger oscillations from 0.05 (at 60 d) to 0.12 dex (at 115 d), a factor of 10 bigger than the errors. Following on from the analysis of SN 2015bn by Nicholl

et al. (2016a) that first highlighted these undulations, it may be that light-curve fluctuations are commonplace in slow-evolving SLSNe I, but that their magnitude is highly variable from object to object. On the other hand, we also checked if such behaviour was present in the fast-evolving SLSNe I. We used data of the well-sampled SNe 2010gx and 2011ke (Pastorello et al. 2010; Inserra et al. 2013) together with LSQ12dlf and SSS120810, which have data up to ∼140 d (Nicholl et al. 2014). We used a linear fit in the case of SN 2010gx, LSQ12dlf and SS120810 and a second-order polynomial in the case of SN 2011ke. The difference in the latter is due to the fact that the SN light curve undergoes a noticeable transition to the tail phase just around ∼50 d (see Inserra et al. 2013), and a linear fit would have produced a bogus oscillation in the residuals. SSS120810 seems to experience a genuine oscillation around ∼70 d, as already noticed by Nicholl et al. (2014), but the rise is sharp and the width is small, especially when compared with the slow-evolving. LSQ12dlf could have experienced an oscillation similar in amplitude to those of before, or alternatively could be the beginning of the tail phase, but the errors and the lack of later data prevent any conclusion. In general, we do not see any clear trend in the residuals resembling those of slow-evolving SLSNe I, even though the time coverage is too short and future work should analyse earlier epochs (e.g. 0 < phase (d) <60) where fast-evolving SLSNe are better sampled.

In the magnetar scenario, light-curve oscillations could be the consequence of the magnetar ionization front. In particular, when O II and O IV layers driven by the hard radiation field of the magnetar reach the ejecta surface, a change of the continuum opacity will happen (Metzger et al. 2014). Lower ionization states generally penetrate further and reach the surface earlier. The less ionized layer should reach the surface in ∼10 d from explosion (well before our detections of the light-curve deviations). The other should happen at the same time of an X-ray shock breakout that, considering the ejecta masses and spin period of slow-evolving SLSNe I, should happen more than a year after peak (see Section 7). Hence, a sudden rise in opacity would be non-trivial to account for and would require a radiative transfer calculation to test the feasibility of this scenario. Multiple changes in opacity, which would be required for SNe 2007bi and 2015bn, would be more difficult to explain.

Another option suggested to explain the pre-peak undulation of SN 2015bn (Nicholl et al. 2016a) is that the fluctuation is powered by oxygen recombination, which would be below 12 000 K (Hatano et al. 1999; Inserra et al. 2013; Quimby et al. 2013), in a similar fashion to what occurs in Type II SNe within the hydrogen layer. Since the oscillations after 50 d already happen at an almost constant temperature of $T_{\rm off} \approx 8000$ K (see Section 5.2), it would be difficult to explain all of them with this interpretation.

On the other hand, oscillations have been observed in SN light curves of interacting transients such as Type Ibn, IIn or SN impostors (e.g. SNe 1998S, 2005ip, 2005la, 2009ip, 2011hw; SNhunt248; Fassia et al. 2000; Pastorello et al. 2008, 2015; Fox et al. 2009; Smith et al. 2009, 2012; Stritzinger et al. 2012; Fraser et al. 2013; Margutti et al. 2014; Kankare et al. 2015; Martin et al. 2015). To reproduce the short time-scale oscillations observed in slow-evolving SLSNe (amplitude of 50–100 d) with ejected masses of 7–16 $M_\odot$ (Chen et al. 2015; Inserra et al. 2016c; Nicholl et al. 2016a) may be difficult since massive ejecta should not produce small-scale changes in the light curve (e.g. Gawryszczak et al. 2010; Fraser et al. 2013). This, together with the small increase in the radius, would disfavour an interaction scenario such as that of pulsational pair-instability SNe (PPISNe) where thermonuclear outbursts due to a recurring pair-instability release of massive shells of material will collide with each other if the latter shells have velocity higher than the initial (Woosley et al. 2007). As a consequence, a viable scenario would need a relatively low mass CSM (<1 $M_\odot$) as that proposed by Moriya et al. (2015) for the late interacting slow-evolving SLSN iPTF13ehe (Yan et al. 2015). Indeed, assuming an average half-period of the fluctuation $t = 25$ d, average luminosity $L = 10^{43}$ erg s^{-1} and $v = 7000$ km s^{-1} (this work; Gal-Yam et al. 2009; Young et al. 2010; Nicholl et al. 2013, 2016a) and using the scaling relation $L \approx M_{\rm CSM} v^2/2t$ (Quimby et al. 2007; Smith & McCray 2007), we find that a CSM of no more than $M_{\rm CSM} \sim 0.04\,M_\odot$ could be responsible for each fluctuation, similar to the findings of SN 2015bn (Nicholl et al. 2016a). If the light-curve oscillations are periodic, they could be the consequence of a close binary system that drives the stripping of the progenitor stars (or the companion) causing a heterogeneous density structure of the CSM (e.g. Weiler et al. 1992; Moriya et al. 2015).

7 X-RAY LIMITS IN SLOW-EVOLVING SLSNE I

An alternative method to investigate the SLSN progenitor scenario and powering mechanism is that of X-ray observations. Both the magnetar and the interaction scenario would predict X-ray emission but at different luminosities and at different phases.

In the case of the magnetar scenario, the pulsar wind inflates a hot cavity behind the expanding stellar ejecta, which is the pulsar wind nebula. Electron/positron pairs cool through synchrotron emission and inverse Compton scattering, producing X-rays inside the nebula. These X-rays ionize the inner regions of the ejecta, driving an ionization front that propagates outwards with time (Metzger et al. 2014). LSQ14an shows a light curve similar to that of SN 2015bn, and hence we can assume similar magnetar and ejecta parameters to those retrieved by Nicholl et al. (2016a, $P = 1.7$–2.1 ms, $B_{14} = 0.9$–1.0 G and $M_{\rm ej} = 8$–$15\,M_\odot$) in their magnetar fit (for the magnetar semi-analytic code, see prescription of Inserra et al. 2013).[10] The mass range is similar to that estimated by other work on slow-evolving SLSNe (Nicholl et al. 2013; Chen et al. 2015), with the only exception of PS1-14bj (Lunnan et al. 2016) showing redder spectra, longer rise time and fainter peak luminosity than the bulk of slow-evolving SLSNe I. Thus, for our analysis, we can use an average mass of 12 $M_\odot$ for LSQ14an, SN 2015bn and in general for all slow-evolving SLSNe I. Following the prescription of Metzger et al. (2014, their equations 5, 6, 56 and A11), we would expect an X-ray breakout of $L_{\rm X} \sim 7.0 \times 10^{42}$ erg s^{-1} at $t_{\rm X} > 700$[11] d from explosion that corresponds to $\gtrsim$630 d from maximum light for an average rise time of about 70 d.

Alternatively, in the interaction scenario, the shock waves created by the interaction between the SN ejecta and the CSM heat gas to X-ray emitting temperatures and can possibly accelerate particles to relativistic energies. The presence of undulations in the light curves would disfavour the presence of a massive CSM (7–19 $M_\odot$; Chatzopoulos et al. 2013; Nicholl et al. 2016a), which would also power the peak luminosity (Chevalier & Irwin 2011). In contrast, a less massive CSM (<1 $M_\odot$, see Section 6) could be more suited to explain LSQ14an and other SLSN I observables. Generally, during

[10] The code is available at https://star.pst.qub.ac.uk/wiki/doku.php/users/ajerkstrand/start

[11] We note that these calculations are highly sensitive to the ejecta mass, which however seems similar for all slow-evolving SLSNe I.

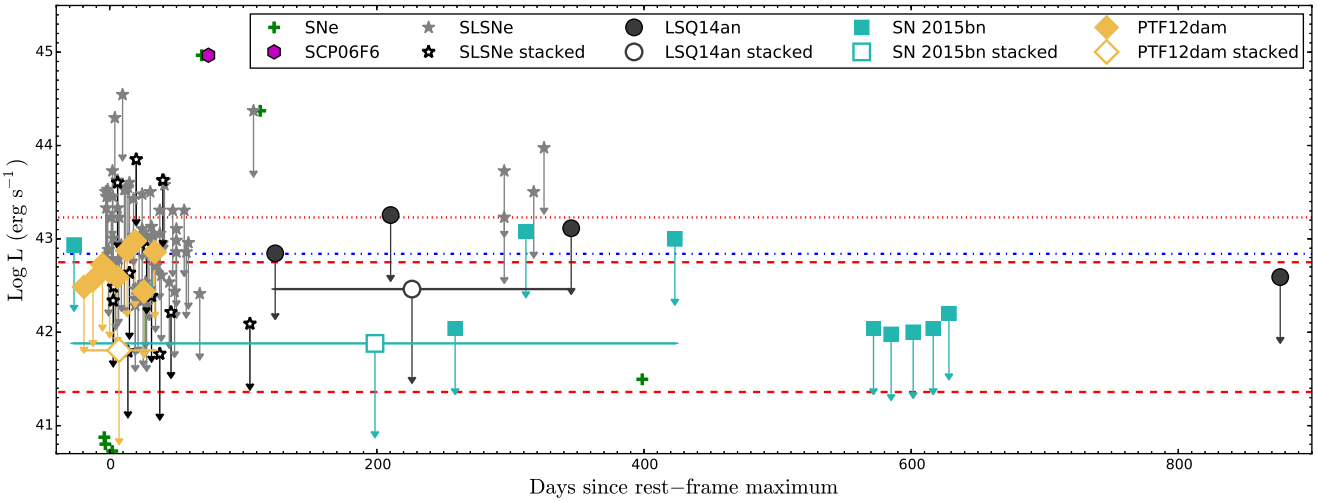

Figure 12. SLSN I X-ray luminosity limits (grey stars) and stacked limits (black open stars) as reported by Levan et al. (2013, but evaluated using the cosmology adopted here), compared with those of the available slow-evolving SLSNe I LSQ14an, SN 2015bn (this work) and PTF12dam (Levan et al. 2013), the single X-ray detection of SLSN I SCP06F6 and a sample of SN detections (Ofek et al. 2013). X-ray limits in the case of breakout from the pulsar nebula ionization front (blue dash–dotted line) and interaction (red dashed lines for the two non-massive CSM cases and red dotted for the massive CSM scenario) are also shown. See the text for further details.

the interaction process between SN ejecta and CSM, the conversion of the kinetic energy into radiation is affected by complicated hydrodynamic and thermal processes including thin shell instabilities (Vishniac 1994), the Rayleigh–Taylor instability of the decelerating cool dense shell (CDS), the CSM clumpiness, mixing, and energy exchange between cold and hot components via radiation and thermal conductivity (Chandra et al. 2015). Here we use a simplified approach in which the X-ray luminosity of both shocks is equal to the total kinetic luminosity times the radiation efficiency ($\alpha_X > 0.1$; Moriya et al. 2013; Chandra et al. 2015). As a consequence, the energy mass relation would be $E \propto M^{0.7}$, assuming an outer power law of the density of the ejecta $n = 10$.

This is equal to $L_X \sim 2.3$–57.3×10^{41} erg s^{-1} for a 0.04–1.0 $M_\odot$ CSM interacting for 200 d (the time when we observe the fluctuations) and to $L_X \sim 1.7 \times 10^{43}$ erg s^{-1} for 13 $M_\odot$ interacting for 400 d, which corresponds to the massive CSM case. In both cases, we assumed $\alpha = 0.1$ and an ejecta always more massive than CSM (e.g. Chatzopoulos et al. 2013; Nicholl et al. 2014). We note that in interacting SNe there is a higher efficiency in the optical (where $\alpha \geq 0.5$; Moriya et al. 2013) than in X-ray (Ofek et al. 2014; Chandra et al. 2015); hence, the highest luminosity achievable in our case would be five times those above. On the other hand, to estimate our X-ray luminosities, we did not consider any photoelectric absorption. In our case, such contribution is hard to evaluate and varies with time, decreasing the soft X-ray output after the start of interaction (see Chevalier & Fransson 2003). This absorption would increase in the case of massive CSM with respect to normal interacting SNe (CSM $\lesssim 1$ $M_\odot$), but the X-ray emission would increase too. Hence, the values reported above have to be treated as higher limits of L_X and they should be similar to the X-ray luminosity emitted around maximum optical light, or soon before that, in the case of interaction with a massive CSM (see Chevalier & Fransson 2003).

We report here the measurements for LSQ14an and SN 2015bn spanning 124–876 d from assumed maximum for the former, and from −27 to 628 d for the latter. In order to place meaningful constraints, we chose observations having at least 4000 s exposure or covering the late phase of the light curve (>300 d since maximum). To date, no observation has been carried out later than those reported here and no X-ray emission has been detected in the data here reported, neither for the stacked images of each SN (evaluated adding all the frames together and assuming an average phase, see Table A5).[12] For both SNe, we assumed the H-column density to the Galactic value [n_H(LSQ14an) $= 4.16 \times 10^{20}$ cm^{-2} and n_H(SN 2015bn) $= 1.22 \times 10^{20}$ cm^{-2}] since SLSNe are hosted in galaxies with little to no internal reddening (see Lunnan et al. 2014; Leloudas et al. 2015a; Perley et al. 2016). We used a generic spectral model with a photon index $\Gamma = 2$ (Levan et al. 2013) to estimate the luminosity limits. We note that limits can change by a factor of ∼3 in flux for a variation of the photon index of the order of 10. We also used a thermal model with $kT = 1.55$ (equal to that used for SCP06F6; Levan et al. 2013, which is the only SLSN detected in X-ray) and hence a factor of 1.2–10 lower than those used in H-rich interacting SNe (e.g. Chandra et al. 2012, 2015; Ofek et al. 2014).

Fig. 12 shows the average limits between the two methods with the power-law method usually resulting in higher luminosities than the thermal one, but still of the same order of magnitude. Only the stacked limits, LSQ14an limit at 876 d, SN 2015bn limit at 259 d and limits at >571 d, are below the magnetar threshold reported above (dot–dashed blue line in Fig. 12). SN 2015bn phase is from ∼400 to ∼30 d earlier than that of the expected ionization front breakout, while LSQ14an is ∼300 d after and the breakout does not last so long at that luminosity. Indeed, it declines with time (see Metzger et al. 2014). However, one needs to be very careful in interpreting the stacked limits in a meaningful way. They are only quantitatively meaningful if they are taken to represent a constant level of flux across the epochs that are stacked. In other words, they by no means rule out time-variable flux between the observed points. All limits are below the X-ray luminosity (dotted red line) that we should have observed in the case of interaction with a dense and massive CSM or collision between two massive shells as

[12] For both SNe, we only stacked the first three epochs since it would have been deceptive to also add the later one, which were carried out from five months to more than a year after the end of our optical campaign.

suggested by the PPISN scenario. However, in the case of a massive CSM, the X-ray luminosity should decrease from peak epoch due to photoelectric absorption (Chevalier & Fransson 2003) and after a year should be a factor of 2–15 less than that at peak. Hence, the late-time limits could not be so constraining.[13] On the other hand, in the case of interaction with a less massive CSM (0.04 $M_\odot$, lower dashed red line), we would have expected an X-ray emission at a similar phase to the fluctuations and hence earlier than 250 d. Such X-ray would have luminosities lower than our limits. This is fulfilled for both limits and stacked limits and all slow-evolving SLSNe. Although we have made many simplifying assumptions, the most simple interpretations is that the X-ray limits disfavour the scenario in which the interaction of ejecta with a massive CSM is the powering mechanism for this SLSN. However, both the magnetar engine and interaction with a less massive CSM could play a role in the spectrophotometric behaviour of slow-evolving SLSNe I.

8 DISCUSSION ON THE CHARACTERISTICS OF SLOW-EVOLVING SLSNE I

The LSQ14an data set is limited to post-peak, but the density of the spectra and light-curve monitoring and the two excellent X-Shooter spectra offer interesting further information to better understand the explosion scenarios of slow-evolving SLSNe I. In summary, it is a slow-evolving SLSN of Type I or Ic. There are a group of, at least, four low-redshift ($z < 0.2$) SLSNe I (or SLSNe Ic) that show very similar spectrophotometric evolution SN 2007bi, PTF12dam, SN 2015bn and LSQ14an. They have very broad light curves that initially (<150 d after peak) decline at a rate similar to ^{56}Co, although it is unlikely that this is the true power source of the luminosity. They have higher redshift analogues such as LSQ14bdq ($z = 0.3450$; Nicholl et al. 2015a), PS1-11ap ($z = 0.5240$; McCrum et al. 2014), DES13S2cmm ($z = 0.6630$; Papadopoulos et al. 2015), iPTF13ajg ($z = 0.7403$; Vreeswijk et al. 2014), SN 2213-1745 and SN 1000+0216 ($z = 2.0458$ and 3.8993, respectively; Cooke et al. 2012). PS1-14bj ($z = 0.5215$; Lunnan et al. 2014) is also similar but has the most extreme in terms of its light-curve width, while iPTF13ehe ($z = 0.3434$; Yan et al. 2015) shows a late-time re-brightening due to interaction with an H-shell (something similar could have happened also to LSQ14bdq; Schulze, private communications). In Sections 4.1 and 4.2, we reported two unusual characteristics of the spectra of LSQ14an, some of which had been observed before, as well as a somewhat common feature in the spectral evolution of this group of SLSNe. Furthermore, in Sections 5 and 6, we described distinctive features of LSQ14an light curves that seem shared by the sample of slow-evolving SLSNe I.

8.1 Spectroscopic characteristics

The first spectroscopic characteristic is the presence of [O III] lines that are significantly broader than the host galaxy, unambiguously formed in the SN ejecta and blueshifted compared to the rest of the ejecta (see Section 4.1 and Table 2). The second is the existence of a strong blueshifted component associated with the prominent [Ca II] line (see Section 4.2).

In LSQ14an and PS1-14bj, the [O III] lines have $v \sim 3000 \pm 300$ km s^{-1}. In the case of LSQ14an, this is significantly lower than that of the bulk of the ejecta as traced by the strong [O I] and O I lines, around 8000 km s^{-1} (Mg I] is broader at ∼12 000 km s^{-1}, although it may be a blend). Furthermore, the density of the [O III] emitting region is likely much less than that where [O I] is formed. This would suggest multiple emitting regions for the above ions. Ionized elements show line profiles much narrower than the neutral ones, strengthening the hypothesis that they come from different regions and likely from a region interior to that where the neutral lines are formed. Since [O I] travel faster than [O III] (see Section 4.1 and Table 2), another possibility is to have a fast, dense outer region and a slow, diffuse region similar to an evacuated inner cavity, which could be another indirect evidence of a magnetar inner engine.

In the magnetar or inner engine scenario, these blueshifted lines and multiple emitting regions could be explained if the ejecta was fragmented or axisymmetric and the observer was in the direction of the axis of symmetry (or both). The latter would happen since only the nearer (blue) component is observed, while red photons would be scattered perpendicular to the observer. An axisymmetric ejecta has been observed for SN 2015bn (Inserra et al. 2016c), while a certain degree of fragmentation, and also asphericity of the ejecta, has been observed in 2D magnetar models (Chen, Woosley & Sukhbold 2016). On the other hand, if we assume a certain degree of interaction with a small amount of material (see Section 6), the blueshift could be due to an additional contribution to the line coming from the CDS, consequence of the shock propagating in the ejecta. This is blueshifted because the CDS is moving at a velocity of ∼1500 km s^{-1} and is optically thick in the continuum; thus, line photons emitted in the red are absorbed by the near side of the CDS (Dessart, Audit & Hillier 2015). Since a high dilution factor is required to model [O III] and [O II] (Jerkstrand et al. 2017), this could be achieved in a diluted interaction region. We already mentioned that [O II] and [O III] lines are much narrower than neutral lines, which in the simplest scenario means an origin in the inner, slower ejecta. Lines from the inner ejecta are normally more prone to obscuration by a residual opacity (a residual 'photosphere'), which can also explain their suppressed red wings. This would be another piece of circumstantial evidence for a hot, ionized inner region and thereby central powering.

Finally, an important point is that the spectra of slow-evolving SLSNe I at 50–70 d surprisingly show almost identical emission features to those seen in the nebular phase at 300–400 d. The spectra at each phase have quite different continuum properties (the early spectra being much bluer), but the ionic transitions are the same. [O I] λλ6300, 6363 significantly increases in strength with time (as expected in CC-SNe), but others such as [Ca II] and [O III] are relatively constant in luminosity. This implies that the line-forming regions of these lines have values of density, temperature and opacity that remain roughly constant over this extended period of evolution. That could also be a consequence of a nearly constant powering mechanism. We see that the emission lines that are redder than 5500 Å show a shift in the centroid of the peak between their values at 50–70 d and those at >300 d (see Fig. 5). For example in SN 2015bn, the [O I] and O I centroids move towards bluer wavelengths, while [Ca II] moves to the red. Multiple emitting regions may thus be present not only in LSQ14an but may be a more common feature in slow-evolving SLSNe I. If slow-evolving SLSNe I are the more massive version of the fast-evolving as suggested by Nicholl et al. (2015b), sharing similar explosion energies and

[13] The photoelectric absorption strongly depends on the column density of the cool gas behind the reverse shock. This is difficult to evaluate in a case of a massive ($\gtrsim$10 $M_\odot$) H- and He-free (or deficient) shell in a sub-solar metallicity environment since it would require assumptions on each term of the formulas. Hence, we avoid any proper calculation of this effect but we would like to warn the reader that photoelectric absorption cannot be ignored and would somehow decrease the X-ray emission at late time.

the same mechanism responsible for the enormous luminosities, we would expect to observe nebular lines later than the fast-evolving, as observed for normal stripped envelope. For example in SN 2009jf, the onset of emission from forbidden calcium is delayed until 85 d from peak (Valenti et al. 2011). However, nebular emission lines (e.g. [O I] or [Ca II]) in fast-evolving SLSNe I have only been observed at ∼150 d after peak (Kangas et al. 2016)[14] and not before ∼100 d (Quimby et al. 2011; Inserra et al. 2013).

Another important characteristic shown by slow-evolving SLSNe I is that their early-time spectra are always bluer than the fast-evolving and the late-time spectra are still remarkably blue even past 200 d (see fig. 7 in Jerkstrand et al. 2017, and Fig. 5 here). They are significantly bluer than stripped envelope SNe, or the faster evolving SLSNe as also noted by Nicholl et al. (2015b, 2016b) for SN 2015bn. That could be explained if we assume a fairly constant 8000 ± 1000 K blackbody type of emission with the observed forbidden and semi-forbidden lines in addition (as seen in the photometric fits in Fig. 10). This type of underlying continuum emission is a common scenario in SNe dominated by interaction; however, in slow-evolving SLSNe I, we still lack the presence of narrow lines forming in the unshocked material. Alternatively, this could be explained by multiple optically thick lines creating a blackbody-like continuum with the forbidden and semi-forbidden lines forming in more external region than those creating the pseudo-blackbody continuum. As highlighted by Jerkstrand et al. (2017), a dense CSM shell of ∼10 $M_\odot$ could reproduce the multiple emission regions and the low filling factor required, but published models are still not able to reproduce the bulk of velocities and the absence of narrow lines.

8.2 Light-curve characteristics

We also highlighted that while the light curve declines at a rate similar to ^{56}Co until 150 d, it increases (for all the objects) from 150 d onwards with a possible further steepening after ∼300 d. The change in decline after 150 d disfavours the pair-instability scenario for slow-evolving SLSNe I since PISN explosion should exhibit full gamma-ray trapping and hence closely follow the decay of ^{56}Co to ^{56}Fe up to 500 d (Jerkstrand et al. 2016). Furthermore, there are some likely real undulations (see Section 6) in the bolometric luminosity. These peculiarities could be present in the higher redshift analogues, but a combination of lower quality data at red wavelengths (observer frame) and late time (rest frame) due to their high redshift prevent a proper investigation.

First of all, we consider the possibility that these features are a consequence of the magnetar scenario. The only possibility would be a change in the density of the ejecta due to the magnetar ionization front, linked to oxygen ionized states (mainly O II and O IV; Metzger et al. 2014), and moving towards the surface of the ejecta. This happens twice but the time-scale is not consistent for both since the former occurs 3–4 weeks after the explosion, while the other at least 700 d after explosion. Moreover, the second is also coincident with an X-ray breakout that has not been observed during the time frame in which we observed the undulations. Secondly, we examine the possibility that the phenomenon is due to some ejecta–CSM interaction. However, even if it is, it is unlikely that this CSM interaction powers the full luminosity of the light curve since our X-ray analysis (see Section 7 for the assumed caveats) does not support the interaction with a massive CSM shell (∼13 $M_\odot$).

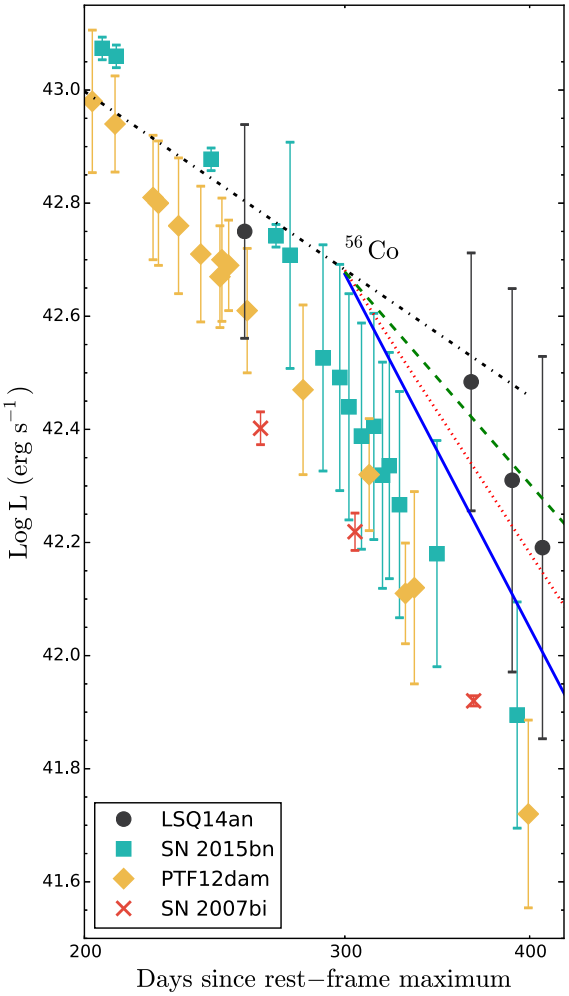

Figure 13. The late-time bolometric evolution of LSQ14an, together with those of slow-evolving SLSNe I SN 2007bi, PTF12dam, SN 2015bn. The green dashed ($n = 3$) and red dotted ($n = 4$) lines show the decline similar to a snowplough phase, while the solid blue line that similar to an adiabatic (Sedov–Taylor) phase. The black dot–dashed line shows the expected ^{56}Co decay. The x-axis is in semi-log scale to highlight the decline and the differences in the power-law indices.

We also see some evidence of an increase in the decline rates after 300 d (see Fig. 13). This is observed in LSQ14an, SN 2015bn and PTF12dam and possibly even SN 2007bi, even though for this object the increase is less certain. This decline is steeper than t^{-3} or t^{-4}, which is known as the snowplough phase, and it has been observed in H-rich interacting SNe (e.g. Fransson et al. 2014; Ofek et al. 2014; Inserra et al. 2016a). Fig. 13 shows that the decline observed in slow-evolving SLSNe I after 300 d seems to follow a power law of t^{-5}, which is the same slope of an adiabatic expansion phase (the Sedov–Taylor phase). This would suggest conservation of energy that, at this time, could be achieved when the density is low enough and the gas cannot cool quickly. An adiabatic expansion at late time of an SN evolution happens when the mass of gas swept up becomes greater than the mass of ejecta and the kinetic energy of the original exploded envelope is transferred to the swept-up gas, and that is heated up by the shock wave. This would require a large amount of interstellar medium or CSM. However, spectra

[14] We note that Kangas et al. (2016) reported that SLSN Gaia16apd shows a fast decline at early phase similar to SNe 2010gx and 2011ke but a late (>130 d) behaviour between the fast- and slow-evolving events.

and X-ray analysis of the sample do not show any of the *primary* observables usually seen in interacting SNe (e.g. narrow lines or X-ray emission).

In the case of LSQ14an, considering a hypothetical rise time from explosion to peak of approximately 70 d (Nicholl et al. 2013, 2016a) and using the simple formalism of $R_{\rm shock} = 2.1 \times 10^{13}\ (E/\rho)^{1/5}\ t^{2/5}$ (Reynolds 2008), where $t = 370$ d from explosion and $\rho \sim 10^8$ (Jerkstrand et al. 2017, and Section 4.1), we derive a distance of 1.2×10^{23} cm for the radius of the shock, which is at least a factor of 10^8 higher than the SN radius. This suggests that it is too early for SLSNe to experience a 'natural' adiabatic phase, which indeed usually happens after 200 yr in normal SNe (Reynolds 2008). The approximate calculation above is also valid (in terms of rough values) for SN 2015bn and PTF12dam. A possible alternative is that these slow-evolving SLSNe experience a further decrease of the gamma-ray trapping (see also Chen et al. 2015; Nicholl et al. 2016b). A further investigation is needed to understand if this behaviour belongs to all slow-evolving SLSNe I and what is the physical reason. We note that none of the fast-evolving SLSNe I discovered up to date has observations at >300 d, which prevent a similar investigation.

9 SUMMARY AND DEDUCTIONS

We have presented an extensive data set on LSQ14an, covering its spectrophotometric behaviour from 55 to 408 d together with X-ray limits spanning over the same time-scale and up to ∼870 d. We show that there are now four well-observed, low-redshift SLSNe I that are similar in their photometric and spectroscopic evolution: SN2007bi, PTF12dam, SN2015bn and LSQ14an. The combination of the data sets provides some new insights into these SNe.

LSQ14an was classified after maximum light and exhibits spectroscopic peculiarities such as broad ($v \sim 3500$ km s^{-1}), blueshifted [O III] λλ4959, 5007 lines, a blueshifted peak of [O II] λλ7320, 7330 (or [O II] + [Ca II] λλ7291, 7323), as well as the late appearance of NIR Ca and the remarkable fact that the lines observed at late time (300–400 d after maximum) are unambiguously shown already at 50 d. The spectra remain surprisingly blue, and the blackbody temperature fits to the photometric flux show a lack of cooling over 300 d. The density ($n_{\rm e} \sim 10^6$ cm^{-3}) and line velocity (v ∼3000 km s^{-1}) of these oxygen features are different from the bulk of ejecta ($n_{\rm e} \sim 10^9$ cm^{-3}, v ∼8000 km s^{-1}), suggesting that multiple emitting regions are responsible for the features observed in the spectra. This could be caused by an axisymmetric or fragmented ejecta or by an additional component arising in a circumstellar material. Furthermore, an in-depth analysis of the light curve shows hints of undulations as observed in other similar SLSNe I (e.g. SN 2015bn), as well a decline faster than ^{56}Co after 150 d and even faster after 300 d (times measured from estimated maximum light). We investigated X-ray upper limits, presenting new limits for LSQ14an and SN 2015bn, and spectrophotometric behaviour with those of nearby slow-evolving SLSNe I showing similar coverage. The deepest limits (not stacked) disfavour the circumstellar interaction with a massive CSM (∼13 M$_\odot$) that is usually needed to reproduce the slow-evolving SLSN light curves.

We noticed that some of these observational features are not unique to LSQ14an but are common in, or even exclusive to, all slow-evolving SLSNe I observed to date.

(i) They show semi-forbidden and forbidden lines from 50–70 d to peak with little to no variation up to 400 d. The strongest evolution is seen in the strengths of the [O I] λλ6300, 6363 lines. The centroids of oxygen and calcium lines appear to move in time. In addition, ionized elements show line profiles different from the neutral ones and likely from a region interior to that where the neutral lines are formed, and where occultation effects can be easily produced. This suggests that multiple emitting regions are responsible for the overall spectra.

(ii) Ca II appears earlier than in broad-lined Type Ic SNe and fast-evolving SLSNe. In two cases (SN 2015bn and LSQ14an), it exhibits a blueshifted peak. In LSQ14an, the line is likely dominated by an [O II] component. The Ca II NIR triplet is observed increasing with time, from 100 d onwards, in contrast to what shown in normal stripped envelope SNe.

(iii) The overall light-curve evolution of these four objects are similar. Initially, all of them decay at a rate consistent with ^{56}Co powering. But after 150 d their bolometric light curves decline faster than the fully trapped ^{56}Co-to-^{56}Fe decay. Moreover, after ∼300 d from maximum light, the bolometric light curves show a further steepening in the decline consistent with a power law of t^{-5}. The light curves overall are not consistent with massive ejecta from PISNe that fully trap the gamma-rays from ^{56}Co decay up to 500 d.

(iv) Light-curve fluctuations seem to be common in the slow-evolving. They can be generally explained with changes in the density structure of the expanding material. Since they appear to occur more than once and at different phases in each object, they are likely due to interaction with a clumpy medium. The medium should have $M < 0.04$ M$_\odot$ to explain the oscillations observed in four out of five inspected slow-evolving SLSNe I and to account for the X-ray limits here reported.

There remains a challenge to explain all these observables, together with those previously reported to date. For example, the observed pre-peak bumps, axisymmetric ejecta, late spectra similar to broad-lined Type Ic and reproducible by ∼10 M$_\odot$ of oxygen (Nicholl et al. 2015a, 2016b; Inserra et al. 2016c; Nicholl & Smartt 2016; Smith et al. 2016; Jerkstrand et al. 2017), with a common scenario. The two most appealing mechanisms for these slow-evolving SLSNe are still central engine (likely a magnetar) and the interaction, even though for the latter some observables are not in agreement with the classical observed behaviour in interacting transients. However, some further considerations can be made. At least a small degree of interaction seems to happen in slow-evolving SLSNe I. If the slow- and fast-evolving SLSNe I share the same nature (i.e. mechanism and maybe progenitor system), the difference between them cannot be due exclusively to a difference in mass as previously suggested (Nicholl et al. 2015b) since that would not reflect the spectral evolution.

To understand if fast- and slow-evolving SLSNe I are a similar or different kind of transients, we need further, and more statistical, investigations. Further studies should also focus on a more detailed early (when we have available both the types) spectra analysis and modelling in order to increase the available information.

ACKNOWLEDGEMENTS

CI thanks Ragnhild Lunnan for sharing the data of PS1-14bj and Stuart Sim for stimulating discussions. This work is based on observations collected at the European Organisation for Astronomical Research in the Southern Hemisphere, Chile as part of PESSTO (the Public ESO Spectroscopic Survey for Transient Objects Survey) ESO programme 188.D-3003, 191.D-0935, 197.D-1075 and the X-Shooter programmes 093.D-0229, 092.D-0555. The research leading to these results has received funding from the European Research Council under the European Union's Seventh Framework

Programme (FP7/2007-2013)/ERC Grant agreement no [291222]. SJS acknowledges funding from STFC grants ST/I001123/1 and ST/L000709/1. CI thanks the organizers and participants of the Munich Institute for Astro- and Particle Physics (MIAPP) workshop 'Supernovae: The Outliers' for stimulating discussions. This research was supported by the Munich Institute for Astro- and Particle Physics (MIAPP) of the DFG cluster of excellence 'Origin and Structure of the Universe'. MF acknowledges the support of a Royal Society – Science Foundation Ireland University Research Fellowship. KM acknowledges support from the STFC through an Ernest Rutherford Fellowship. TWC and TK acknowledge the support through the Sofia Kovalevskaja Award to P. Schady from the Alexander von Humboldt Foundation of Germany. The Liverpool Telescope is operated on the island of La Palma by Liverpool John Moores University in the Spanish Observatorio del Roque de los Muchachos of the Instituto de Astrofisica de Canarias with financial support from the UK Science and Technology Facilities Council. The Pan-STARRS1 Surveys (PS1) have been made possible through contributions of the Institute for Astronomy, the University of Hawaii, the Pan-STARRS Project Office, the Max Planck Society and its participating institutes, the Max Planck Institute for Astronomy, Heidelberg and the Max Planck Institute for Extraterrestrial Physics, Garching, the Johns Hopkins University, Durham University, the University of Edinburgh, Queen's University Belfast, the Harvard-Smithsonian Center for Astrophysics, the Las Cumbres Observatory Global Telescope Network Incorporated, the National Central University of Taiwan, the Space Telescope Science Institute, the National Aeronautics and Space Administration under Grant No. NNX08AR22G issued through the Planetary Science Division of the NASA Science Mission Directorate, the National Science Foundation under Grant No. AST-1238877, the University of Maryland, and Eotvos Lorand University (ELTE) and the Los Alamos National Laboratory.

REFERENCES

Agnoletto I. et al., 2009, ApJ, 691, 1348
Alard C., 2000, A&AS, 144, 363
Amorín R., Pérez-Montero E., Vílchez J. M., Papaderos P., 2012, ApJ, 749, 185
Angus C. R., Levan A. J., Perley D. A., Tanvir N. R., Lyman J. D., Stanway E. R., Fruchter A. S., 2016, MNRAS, 458, 84
Asplund M., Grevesse N., Sauval A. J., Scott P., 2009, ARA&A, 47, 481
Baltay C. et al., 2013, PASP, 125, 683
Benetti S. et al., 2014, MNRAS, 441, 289
Bianco F. B., Modjaz M., Oh S. M., Fierroz D., Liu Y. Q., Kewley L., Graur O., 2016, Astron. Comput., 16, 54
Chandra P., Chevalier R. A., Chugai N., Fransson C., Irwin C. M., Soderberg A. M., Chakraborti S., Immler S., 2012, ApJ, 755, 110
Chandra P., Chevalier R. A., Chugai N., Fransson C., Soderberg A. M., 2015, ApJ, 810, 32
Chatzopoulos E., Wheeler J. C., Vinko J., Horvath Z. L., Nagy A., 2013, ApJ, 773, 76
Chen T.-W. et al., 2015, MNRAS, 452, 1567
Chen T.-W., Smartt S. J., Yates R. M., Nicholl M., Krühler T., Schady P., Dennefeld M., Inserra C., 2016, MNRAS, preprint (arXiv:1605.04925)
Chen K.-J., Woosley S. E., Sukhbold T., 2016, ApJ, 832, 73
Chevalier R. A., Fransson C., 1992, ApJ, 395, 540
Chevalier R. A., Fransson C., 2003, in Weiler K., ed., Lecture Notes in Physics, Vol. 598, Supernovae and Gamma-Ray Bursters. Springer-Verlag, Berlin, p. 171
Chevalier R. A., Irwin C. M., 2011, ApJ, 729, L6
Chomiuk L. et al., 2011, ApJ, 743, 114
Cooke J. et al., 2012, Nature, 491, 228
da Cunha E., Charlot S., Elbaz D., 2008, MNRAS, 388, 1595
Dessart L., Hillier D. J., Waldman R., Livne E., Blondin S., 2012, MNRAS, 426, L76
Dessart L., Audit E., Hillier D. J., 2015, MNRAS, 449, 4304
Dexter J., Kasen D., 2013, ApJ, 772, 30
Fassia A. et al., 2000, MNRAS, 318, 1093
Filippenko A. V. et al., 1995, ApJ, 450, L11
Fox O. et al., 2009, ApJ, 691, 650
Fransson C. et al., 2002, ApJ, 572, 350
Fransson C. et al., 2014, ApJ, 797, 118
Fraser M. et al., 2013, MNRAS, 433, 1312
Gal-Yam A., 2012, Science, 337, 927
Gal-Yam A. et al., 2007, ApJ, 656, 372
Gal-Yam A. et al., 2009, Nature, 462, 624
Gawryszczak A., Guzman J., Plewa T., Kifonidis K., 2010, A&A, 521, A38
Gezari S. et al., 2009, ApJ, 690, 1313
Gonzalez-Delgado R. M. et al., 1994, ApJ, 437, 239
Hatano K., Branch D., Fisher A., Millard J., Baron E., 1999, ApJS, 121, 233
Howell D. A. et al., 2013, ApJ, 779, 98
Hunter D. J. et al., 2009, A&A, 508, 371
Inserra C., Smartt S. J., 2014, ApJ, 796, 87
Inserra C. et al., 2011, MNRAS, 417, 261
Inserra C. et al., 2013, ApJ, 770, 128
Inserra C. et al., 2016a, MNRAS, 459, 2721
Inserra C. et al., 2016b, ApJ, preprint (arXiv:1604.01226)
Inserra C., Bulla M., Sim S. A., Smartt S. J., 2016c, ApJ, 831, 79
Jerkstrand A., Ergon M., Smartt S. J., Fransson C., Sollerman J., Taubenberger S., Bersten M., Spyromilio J., 2015, A&A, 573, A12
Jerkstrand A., Smartt S. J., Heger A., 2016, MNRAS, 455, 3207
Jerkstrand A. et al., 2017, ApJ, 835, 13
Kangas T. et al., 2016, MNRAS, preprint (arXiv:1611.10207)
Kankare E. et al., 2015, A&A, 581, L4
Kasen D., Bildsten L., 2010, ApJ, 717, 245
Kennicutt R. C., Jr, 1998, ARA&A, 36, 189
Kirshner R. P., Morse J. A., Winkler P. F., Blair W. P., 1989, ApJ, 342, 260
Kozyreva A., Blinnikov S., 2015, MNRAS, 454, 4357
Krühler T. et al., 2015, A&A, 581, A125
Leget P.-F. et al., 2014, Astron. Telegram, 5718
Leloudas G. et al., 2015a, MNRAS, 449, 917
Leloudas G. et al., 2015b, ApJ, 815, L10
Levan A. J., Read A. M., Metzger B. D., Wheatley P. J., Tanvir N. R., 2013, ApJ, 771, 136
Liu Y.-Q., Modjaz M., 2016, ApJ, preprint (arXiv:1612.07321)
Lunnan R. et al., 2014, ApJ, 787, 138
Lunnan R. et al., 2016, ApJ, 831, 144
McCrum M. et al., 2014, MNRAS, 437, 656
McCrum M. et al., 2015, MNRAS, 448, 1206
Magnier E. A. et al., 2013, ApJS, 205, 20
Margutti R. et al., 2014, ApJ, 780, 21
Martin J. C., Hambsch F.-J., Margutti R., Tan T. G., Curtis I., Soderberg A., 2015, AJ, 149, 9
Mazzali P. A., Sullivan M., Pian E., Greiner J., Kann D. A., 2016, MNRAS, 458, 3455
Metzger B. D., Vurm I., Hascoët R., Beloborodov A. M., 2014, MNRAS, 437, 703
Milisavljevic D., Fesen R. A., Gerardy C. L., Kirshner R. P., Challis P., 2010, ApJ, 709, 1343
Miller A. A. et al., 2009, ApJ, 690, 1303
Modigliani A. et al., 2010, Proc. SPIE, 7737, 773728
Moriya T. J., Blinnikov S. I., Baklanov P. V., Sorokina E. I., Dolgov A. D., 2013, MNRAS, 430, 1402
Moriya T. J., Liu Z.-W., Mackey J., Chen T.-W., Langer N., 2015, A&A, 584, L5
Nicholl M., Smartt S. J., 2016, MNRAS, 457, L79
Nicholl M. et al., 2013, Nature, 502, 346

Nicholl M. et al., 2014, MNRAS, 444, 2096
Nicholl M. et al., 2015a, ApJ, 807, L18
Nicholl M. et al., 2015b, MNRAS, 452, 3869
Nicholl M. et al., 2016a, ApJ, 826, 39
Nicholl M. et al., 2016b, ApJ, 828, L18
Nicholls D. C., Dopita M. A., Sutherland R. S., Kewley L. J., Palay E., 2013, ApJS, 207, 21
Ofek E. O. et al., 2007, ApJ, 659, L13
Ofek E. O. et al., 2013, ApJ, 763, 42
Ofek E. O. et al., 2014, ApJ, 781, 42
Osterbrock D. E., Ferland G. J., 2006, Astrophysics of Gaseous Nebulae and Active Galactic Nuclei, 2nd edn. University Science Books, Sausalito, CA
Papadopoulos A. et al., 2015, MNRAS, 449, 1215
Pastorello A. et al., 2008, MNRAS, 389, 131
Pastorello A. et al., 2010, ApJ, 724, L16
Pastorello A. et al., 2015, MNRAS, 449, 1954
Patat F. et al., 2001, ApJ, 555, 900
Perley D. A. et al., 2016, ApJ, 830, 13
Pettini M., Pagel B. E. J., 2004, MNRAS, 348, L59
Pignata G. et al., 2004, MNRAS, 355, 178
Poole T. S. et al., 2008, MNRAS, 383, 627
Pozzo M., Meikle W. P. S., Fassia A., Geballe T., Lundqvist P., Chugai N. N., Sollerman J., 2004, MNRAS, 352, 457
Prajs S. et al., 2017, MNRAS, 464, 3568
Quimby R. M., Aldering G., Wheeler J. C., Höflich P., Akerlof C. W., Rykoff E. S., 2007, ApJ, 668, L99
Quimby R. M. et al., 2011, Nature, 474, 487
Quimby R. M., Yuan F., Akerlof C., Wheeler J. C., 2013, MNRAS, 431, 912
Reynolds S. P., 2008, ARA&A, 46, 89
Schlafly E. F., Finkbeiner D. P., 2011, ApJ, 737, 103
Schlafly E. F. et al., 2012, ApJ, 756, 158
Schulze S. et al., 2016, preprint (arXiv:1612.05978)
Scovacricchi D., Nichol R. C., Bacon D., Sullivan M., Prajs S., 2016, MNRAS, 456, 1700
Smartt S. J. et al., 2015, A&A, 579, A40
Smith N., McCray R., 2007, ApJ, 671, L17
Smith N. et al., 2007, ApJ, 666, 1116
Smith N. et al., 2009, ApJ, 695, 1334
Smith N., Mauerhan J. C., Silverman J. M., Ganeshalingam M., Filippenko A. V., Cenko S. B., Clubb K. I., Kandrashoff M. T., 2012, MNRAS, 426, 1905
Smith M. et al., 2016, ApJ, 818, L8
Stritzinger M. et al., 2002, AJ, 124, 2100
Stritzinger M. et al., 2012, ApJ, 756, 173
Taubenberger S. et al., 2009, MNRAS, 397, 677
Tonry J. L. et al., 2012, ApJ, 750, 99
Valenti S. et al., 2011, MNRAS, 416, 3138
Vishniac E. T., 1994, ApJ, 428, 186
Vreeswijk P. M. et al., 2014, ApJ, 797, 24
Vreeswijk P. M. et al., 2017, ApJ, 835, 58
Weiler K. W., van Dyk S. D., Pringle J. E., Panagia N., 1992, ApJ, 399, 672
Wheeler J. C., Benetti S., 2000, Allen's Astrophysical Quantities, 4th edn. Am. Inst. Phys., New York, p. 451
Woosley S. E., 2010, ApJ, 719, L204
Woosley S. E., Blinnikov S., Heger A., 2007, Nature, 450, 390
Yan L. et al., 2015, ApJ, 814, 108
Yaron O., Gal-Yam A., 2012, PASP, 124, 668
Young D. R. et al., 2010, A&A, 512, A70

APPENDIX A: TABLES

Table A1. Journal of spectroscopic observations of LSQ14an.

Date yy/mm/dd	MJD	Phase[a] (d)	Range (observer frame) (Å)	Range (rest frame) (Å)	Resolution (Å)	Instrumental configuration
14/01/02	56660.31	55.0	3665–9285	3150–7980	18	NTT+EFOSC2+gm13
14/01/08	56665.81	59.7	3360–10 010	2890–8600	14/13	NTT+EFOSC2+gm11/16
14/01/29	56687.28	78.2	3095–24 785	2660–21 300	1.0/1.1/3.3	VLT+X-Shooter+UV/OPT/NIR
14/01/29	56687.31	78.2	3360–10 010	2890–8600	14/13	NTT+EFOSC2+gm11/16
14/02/21	56710.70	98.3	3360–10 010	2890–8600	14/13	NTT+EFOSC2+gm11/16
14/03/08	56725.16	110.7	3665–9285	3150–7980	18	NTT+EFOSC2+gm13
14/04/22	56770.02	149.3	3665–9285	3150–7980	18	NTT+EFOSC2+gm13
14/06/21	56829.09	200.0	3095–24 785	2660–21 300	1.0/1.1/3.3	VLT+X-Shooter+UV/OPT/NIR
14/08/21	56890.49	252.8	3665–9285	3150–7980	18	NTT+EFOSC2+gm13

Note. [a]Phase with respect to the assumed maximum.

Table A2. *gri* light curves of LSQ14an.

Date yy/mm/dd	MJD	Phase[a] (d)	*g*	*r*	*i*	Instrument[b]
14/01/02	56659.28	54.1		18.60 (0.08)		LSQ
14/01/04	56661.28	55.8		18.62 (0.08)		LSQ
14/01/06	56663.30	57.6		18.64 (0.08)		LSQ
14/01/14	56672.19	65.2	18.93 (0.13)	18.92 (0.19)	18.89 (0.17)	LT
14/01/28	56686.23	77.3	19.15 (0.11)	19.12 (0.11)	18.99 (0.12)	LT
14/02/01	56689.24	79.9	19.12 (0.13)	19.13 (0.14)	18.99 (0.12)	NTT
14/02/07	56696.24	85.9	19.11 (0.17)	19.14 (0.11)	19.09 (0.12)	LT
14/02/13	56702.11	90.9	19.19 (0.16)	19.13 (0.14)	19.24 (0.15)	LT
14/03/12	56729.03	114.1	19.35 (0.18)	19.36 (0.14)	19.40 (0.16)	LT
14/04/21	56769.17	148.6	19.68 (0.12)	20.02 (0.14)	19.83 (0.12)	NTT
14/05/16	56793.93	169.8	20.06 (0.14)	20.13 (0.14)	20.13 (0.14)	LT
14/05/19	56796.89	172.4	20.03 (0.12)	20.19 (0.12)	20.18 (0.13)	LT
14/05/23	56800.88	175.8	20.11 (0.12)	20.32 (0.12)	20.45 (0.14)	LT
14/05/27	56804.91	179.3	20.07 (0.11)	20.41 (0.12)	20.49 (0.14)	LT
14/06/03	56811.96	185.3	20.07 (0.12)	20.46 (0.13)	20.55 (0.15)	LT
14/08/25	56894.99	256.7	21.55 (0.11)	21.46 (0.14)	21.60 (0.23)	NTT
14/12/29	57021.30	365.2	22.50 (0.13)	22.49 (0.15)	22.82 (0.19)	NTT
15/01/26	57049.30	389.3	22.98 (0.15)	23.03 (0.19)	23.18 (0.25)	NTT
15/02/17	57071.20	408.1	23.64 (0.19)	23.83 (0.22)	24.06 (0.32)	NTT

Notes. [a]Phase with respect to the assumed maximum.
[b]LSQ = La Silla QUEST; LT = Liverpool Telescope + IO:O; NTT = ESO NTT + EFOSC2.

Table A3. *BVRJHK* light curve of LSQ14an measured after template subtraction (from 2015-04-17) using HOTPANTS.

Date yy/mm/dd	MJD	Phase[a] (d)	*B*	*V*	*R*	Instrument[b]
14/01/02	56660.31	55.0		19.00 (0.10)		NTT
14/01/08	56665.81	59.7		19.10 (0.13)		NTT
14/01/29	56687.28	78.2		19.49 (0.09)		NTT
14/02/21	56710.70	98.3		19.63 (0.12)		NTT
14/03/08	56725.16	110.7		19.68 (0.18)		NTT
14/04/22	56770.02	149.3		20.13 (0.14)		NTT
14/08/25	56894.99	256.7	21.85 (0.10)	21.50 (0.03)	21.31 (0.09)	NTT
14/12/29	57021.30	365.2	22.72 (0.15)	22.47 (0.06)	22.39 (0.10)	NTT
15/01/26	57049.30	389.3	23.21 (0.13)	22.99 (0.10)	22.93 (0.15)	NTT
15/02/17	57071.20	408.1	23.95 (0.20)	23.46 (0.16)	23.84 (0.19)	NTT
Date yy/mm/dd	MJD	Phase[a] (d)	*J*	*H*	*K*	Instrument[b]
14/04/23	56771.04	150.16	19.93 (0.12)	20.04 (0.12)	20.08 (0.20)	NTT

Notes. [a]Phase with respect to the assumed maximum.
[b]NTT = ESO NTT + EFOSC2.

Table A4. Magnitudes in *griBVR* of the local sequence stars in the field of LSQ14an.

RA	Dec.	*g*	*r*	*i*
12:53:52.095	−29:32:20.47	16.36 (0.05)	15.92 (0.05)	15.74 (0.05)
12:53:49.806	−29:31:58.25	17.61 (0.07)	16.37 (0.05)	15.56 (0.05)
12:53:49.136	−29:32:15.38	17.11 (0.05)	16.61 (0.04)	16.38 (0.04)
12:53:48.019	−29:31:37.48	17.78 (0.07)	16.51 (0.04)	15.67 (0.05)
12:53:44.110	−29:32:04.44	16.76 (0.06)	16.32 (0.05)	16.13 (0.05)
12:53:52.622	−29:29:23.17	16.38 (0.05)	15.93 (0.04)	15.75 (0.05)
12:53:52.300	−29:29:36.81	16.22 (0.05)	15.59 (0.04)	15.27 (0.05)
12:53:44.595	−29:29:30.65	17.76 (0.08)	17.22 (0.04)	16.98 (0.03)
RA	Dec.	*B*	*V*	*R*
12:53:52.672	−29:30:12.65	20.56 (0.13)	19.60 (0.08)	18.95 (0.07)
12:53:40.273	−29:30:15.14	19.35 (0.12)	18.52 (0.10)	18.02 (0.10)
12:53:40.049	−29:30:54.67	18.93 (0.11)	18.22 (0.09)	17.76 (0.09)
12:53:44.735	−29:31:10.91	20.88 (0.12)	20.41 (0.10)	20.04 (0.08)
12:53:47.986	−29:31:37.54	18.62 (0.14)	17.16 (0.10)	16.19 (0.08)
12:53:49.102	−29:32:15.83	17.67 (0.13)	16.95 (0.10)	16.48 (0.08)
12:53:55.383	−29:32:04.58	20.59 (0.14)	20.00 (0.10)	19.62 (0.09)

Table A5. Log of X-ray observations of LSQ14an and SN 2015bn.

			LSQ14an		
Date yy/mm/dd	MJD	Phase[a] (d)	Exposure (s)	F_X (erg cm^{-2} s^{-1})	L_X (erg s^{-1})
14/03/24	56740.52	123.9	9000	<1.0e−13	<7.0e42
14/07/03	56841.04	210.3	5400	<2.6e−13	<1.8e43
14/12/07	56998.41	345.5	7600	<1.8e−13	<1.3e43
16/08/16	57616.01	876.3	9500	<5.6e−14	<3.9e42
Stacked					
	56859.70[b]	226.3[b]	22 000	<4.1e−14	<2.9e42
			SN 2015bn		
Date yy/mm/dd	MJD	Phase[a] (d)	Exposure (s)	F_X (erg cm^{-2} s^{-1})	L_X (erg s^{-1})
15/02/19	57072.29	− 26.7	6000	<2.7e−13	<8.6e42
15/04/19	57131.26	26.3	6700	<8.7e−14	<2.8e42
16/01/03	57390.02	258.6	8700	<3.6e−14	<1.1e42
16/03/02	57449.07	311.6	2800	<3.7e−13	<1.2e43
16/07/04	57573.21	423.1	3900	<3.2e−13	<1.0e43
16/12/16	57738.87	571.8	8900	<3.6e−14	<1.1e42
16/12/31	57753.58	585.0	9940	<3.0e−14	<9.5e41
17/01/19	57772.01	601.5	9920	<3.2e−14	<1.0e42
17/02/06	57788.56	616.5	8950	<3.5e−14	<1.1e42
17/02/17	57801.71	628.3	8900	<5.0e−14	<1.6e42
Stacked					
	57323.17[c]	198.6[c]	28 000	<2.4e−14	<7.6e41

Notes. [a]Phase with respect to the assumed maximum.
[b]Average date/MJD between the first three exposures.
[c]Average date/MJD between the first four exposures.

Table A6. Observed emission line measurements of the host galaxy of LSQ14an from the spectrum taken by VLT + X-Shooter at +200.0 d (not applying any reddening corrections). The EW of each line is a minimum, not a real line strength due to the SN contamination of the continuum.

Line	λ (Å)	Observed flux (10^{-17} erg s^{-1} cm^{-2})	Error (10^{-17} erg s^{-1} cm^{-2})	rms (10^{-17} erg s^{-1} cm^{-2})	EW (Å)	FWHM (Å)
He I	3188	3.92	1.98	0.52	0.55	1.88
He I	3704	1.43	0.91	0.29	0.20	1.29
[O II]	3726	65.65	2.39	0.42	8.94	1.64
[O II]	3729	92.03	2.69	0.42	12.46	1.63
H12	3750	1.22	1.03	0.34	0.16	1.24
H11	3770	1.70	0.98	0.32	0.23	1.24
H10	3798	2.89	0.73	0.23	0.43	1.28
H9	3835	6.79	1.44	0.37	0.91	1.76
[Ne III]	3868	34.63	1.76	0.37	4.51	1.54
He I+H8	3889	12.27	0.96	0.25	1.65	1.50
[Ne III]	3967	7.40	0.93	0.27	0.94	1.36
H7	3969	9.65	0.95	0.27	1.23	1.36
[N II]+He I	4026	0.82	0.44	0.16	0.12	1.00
H δ	4102	17.14	0.90	0.22	2.88	1.54
H γ	4340	35.26	1.29	0.24	5.16	1.86
[O III]	4363	5.43	1.03	0.30	0.82	1.86
He I	4471	4.35	0.87	0.20	0.86	2.44
H β	4861	68.47	2.06	0.24	22.68	2.03
[O III]	4959	129.20	3.10	0.37	23.43	1.96
[O III]	5007	345.70	4.65	0.34	68.15	2.03
He I	5876	7.75	0.57	0.11	4.90	2.25
[O I]	6300	4.88	0.96	0.19	2.12	2.90
[S III]	6312	1.56	0.85	0.18	0.65	2.90
[O I]	6364	1.36	0.43	0.11	0.51	2.15
[N II]	6548	2.11	1.61	0.35	1.01	2.73
H α	6563	234.30	3.37	0.20	105.19	2.73
[N II]	6584	5.25	0.54	0.11	2.67	2.73
He I	6678	1.96	0.33	0.07	1.43	2.72
[S II]	6717	13.83	0.78	0.11	10.87	2.74
[S II]	6731	10.21	0.68	0.11	8.19	2.74
He I	7065	1.87	0.41	0.09	1.36	2.75
[Ar III]	7136	4.89	1.16	0.22	3.10	2.82
[O II]	7320	0.95	0.51	0.12	0.19	2.47
[O II]	7330	1.05	0.52	0.12	0.21	2.47
[S III]	9069	15.74	1.05	0.15	10.96	3.28
[S III]	9532	36.59	2.86	0.31	24.45	3.42

This paper has been typeset from a TEX/LATEX file prepared by the author.